Incorporation of Diffusion Tensor MRI in Non-Rigid Registration for Image-Guided Neurosurgery

by

Corey Ann Kemper

Submitted to the Department of Electrical Engineering and Computer Science
in partial fulfillment of the requirements for the degree of

Master of Science in Computer Science and Engineering

at the

MASSACHUSETTS INSTITUTE OF TECHNOLOGY

June 2003

Author .....
Department of Electrical Engineering and Computer Science
May 8, 2003

Certified by .....
W. E. L. Grimson
Bernard Gordon Professor of Medical Engineering
Thesis Supervisor

Certified by .....
Simon K. Warfield
Assistant Professor of Radiology, Harvard Medical School
Thesis Supervisor

Accepted by .....
Arthur C. Smith
Chairman, Department Committee on Graduate Students

Incorporation of Diffusion Tensor MRI in Non-Rigid Registration for Image-Guided Neurosurgery

by

Corey Ann Kemper

Submitted to the Department of Electrical Engineering and Computer Science
on May 8, 2003, in partial fulfillment of the
requirements for the degree of
Master of Science in Computer Science and Engineering

Abstract

The development of image-guided neurosurgery methods over the past decade has permitted major advances in minimally invasive therapy. A variety of imaging techniques provide vital information about the internal structure of the brain to the neurosurgeon, such as the locations of blood vessels, white matter tracts and regions of cortical function. Time constraints during a neurosurgical procedure, however, limit the intraoperative image acquisitions to low resolution, anatomical scans. Therefore, in order to combine preoperative images with the updated scans for visualization, accurate registration is necessary. The opening of the skull and the dura, as well as resection of the tumor, causes the brain to deform non-rigidly. It has been determined previously that a suitable way to model these deformations is via a biomechanical model that treats the brain as a homogeneous, isotropic, linear elastic solid. The calculated deformation is then applied to all the available preoperative images. This thesis extends the biomechanical model-based non-rigid registration algorithm to apply deformations to diffusion tensor magnetic resonance images (DT-MRI) and takes into account the underlying white matter structure derived from them in an attempt to better model the brain. DT-MRI provides magnitude and directional information of the diffusion of water, which has been shown to correspond to the anisotropy of the brain tissue. This is then used to compute anisotropic, local material parameters as inputs to the model. Experiments performed on synthetic data and retrospective surgical cases were used to evaluate the results of the registration algorithm across a range of elasticity parameters and in comparison to the earlier model.

Thesis Supervisor: W. E. L. Grimson
Title: Bernard Gordon Professor of Medical Engineering

Thesis Supervisor: Simon K. Warfield
Title: Assistant Professor of Radiology, Harvard Medical School

Acknowledgments

First, I would like acknowledge the support and guidance of Dr. Eric Grimson, my advisor at MIT. I so appreciate his help in exploring thesis projects, deciding on research goals, and revising this thesis. He has made the research group a great place to work.

The guidance of Dr. Simon Warfield, my advisor at the Surgical Planning Laboratory, was also invaluable. In addition to the high-level ideas, he helped with so many of the practical implementation details.

Many thanks to Dr. Ion-Florin Talos for providing the seemingly endless manual registrations, segmentations, and landmark identifications that required his expertise, as well as contributing a clinical perspective.

Thanks to all others at the SPL, especially Dr. Ron Kikinis, for much helpful advice, and Dr. Steve Haker, for figuring out math problems that stumped me. Also, thanks to everyone who has added features to and maintained the Slicer software, and to those whose work I have extended directly, Dr. Matthieu Ferrant and Alida Tei. Their documentation made my life so much easier.

All of those in the Vision Group at MIT have made me feel so welcome over the last two years and have always made themselves available to answer questions and give advice. A special thanks to Lauren O'Donnell for spending a lot of time helping me to understand DT-MRI and double-checking my results. The moral support provided by everyone has been so important to me the past few months especially.

Finally, thanks to the Whitaker Foundation for the financial support provided by a graduate fellowship.

Contents

List of Figures

List of Tables

Chapter 1

Introduction

1.1 Motivation

Medical imaging has played an increasingly important role in surgical planning and treatment because it provides valuable information about anatomical structure and function. This has been particularly helpful for neurosurgical procedures, where the surgeon is faced with the challenge of removing as much tumor as possible without damaging the healthy brain tissue surrounding it. Because healthy and diseased brain tissue often appears visually similar, and because critical structures underneath the brain surface are not visible as it is being cut, tumor resection is a daunting task. Vital anatomical information, such as the orientation and location of dense white matter fiber bundles, may not be visible at all. Regions important to function are often visually indistinguishable and may have been displaced or even infiltrated by the growth of the tumor. However, an abundance of information is available to the neurosurgeon from data derived from a variety of imaging modalities that can address these difficulties.

The development of image-guided neurosurgery (IGNS) methods over the past decade has permitted major advances in minimally invasive therapy delivery [7, 12, 16, 18, 19, 33, 42, 43]. These techniques, carried out in operating rooms equipped with special purpose imaging devices, such as the open magnet system at the Surgical Planning Laboratory at the Brigham and Women's Hospital (Figure 1-1), allow

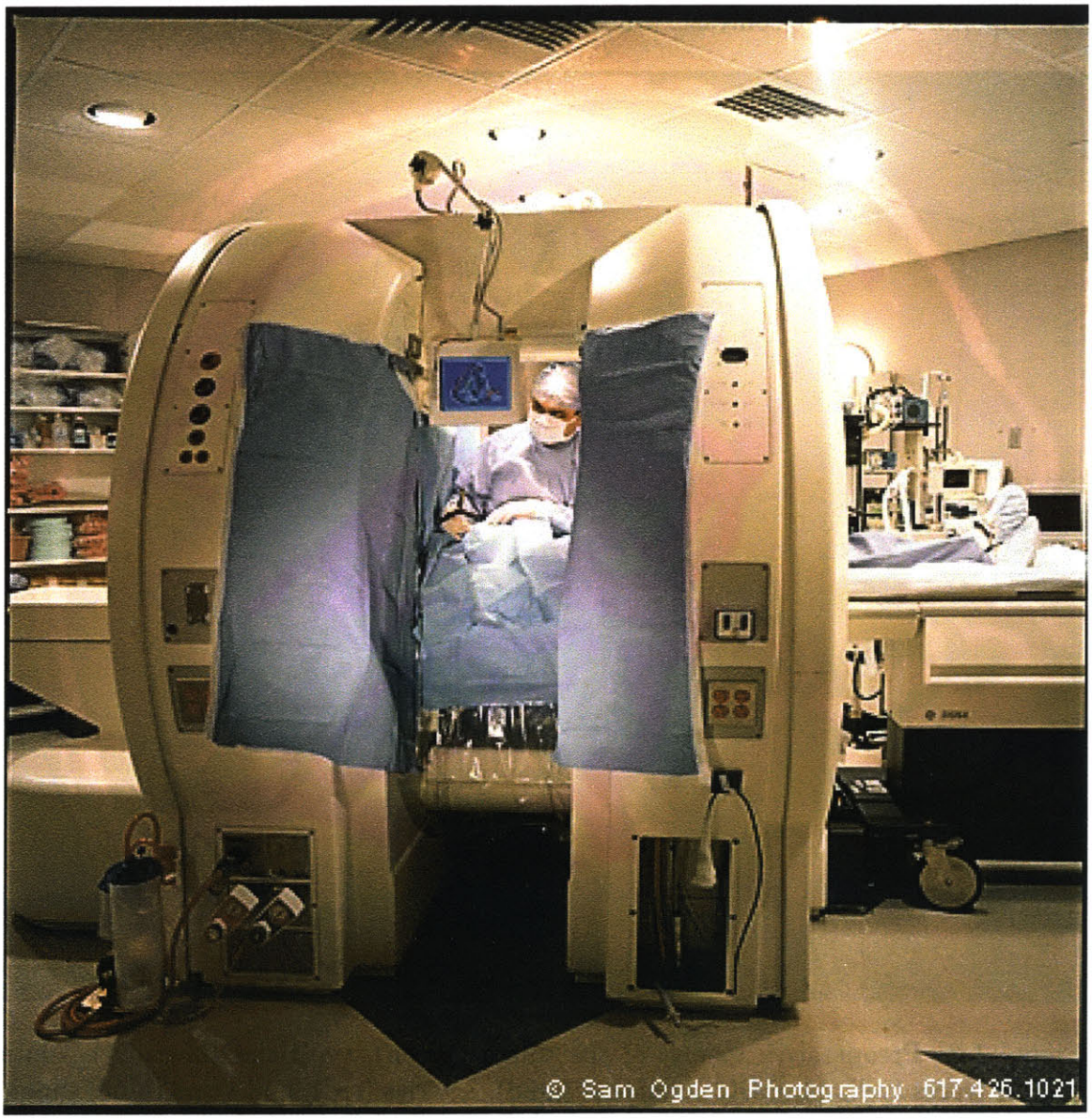

Figure 1-1: A photo of the open magnet system (*http://www.slicer.org*)

surgeons to look at updated images acquired during the procedure, which give the surgeon a better understanding of the current locations of the deeper structures of the brain. A number of imaging modalities have been used for image guidance; MRI has an important advantage over other modalities due to its high spatial resolution and superior soft tissue contrast, which has proven to be particularly useful for IGNS.

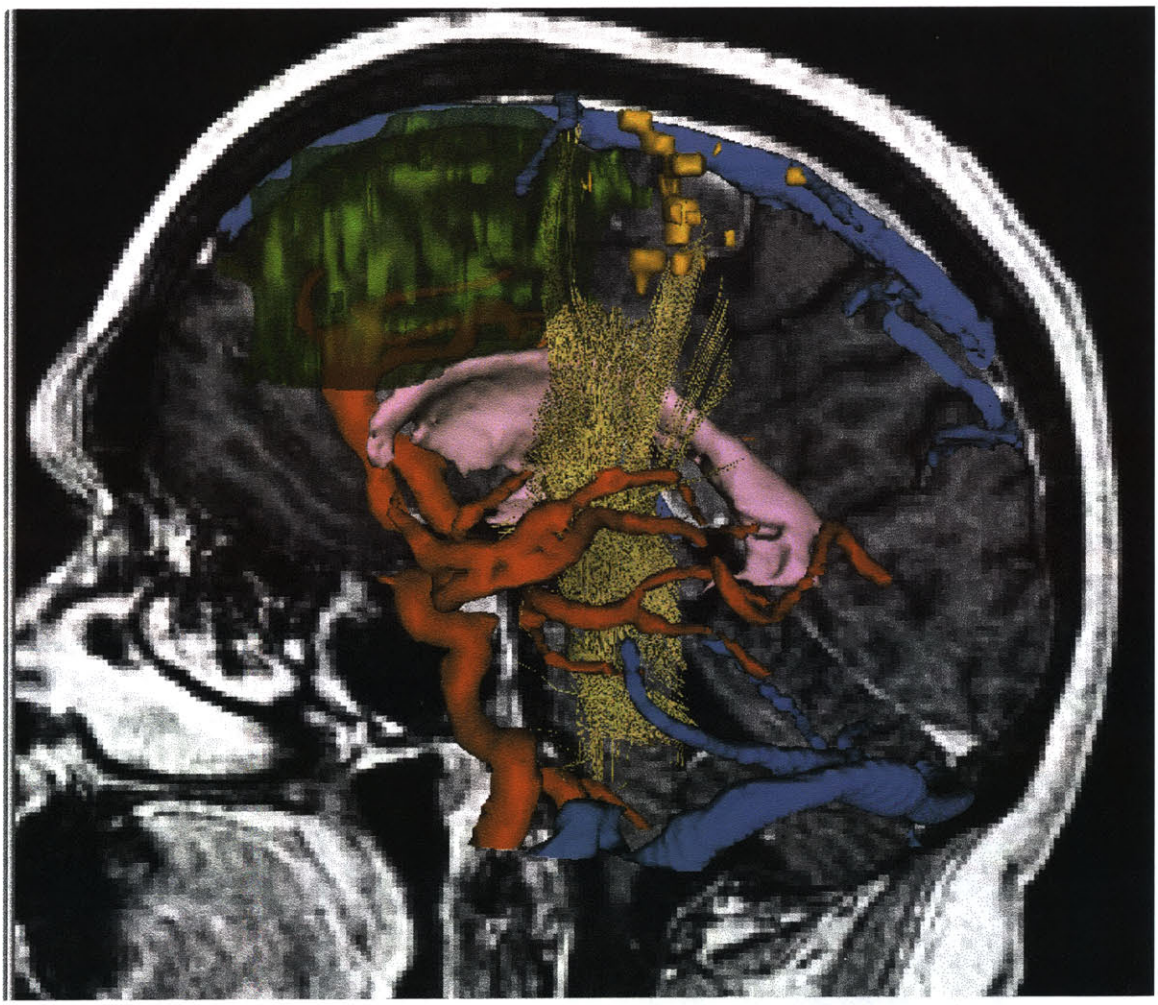

Figure 1-2: Preoperative models of the tumor (green), ventricles (lavender), white matter tracts (yellow), fMRI activation (gold), arteries (red), and veins (blue) superimposed on a sagittal slice of a grey-scale MRI image.

Due to the time constraints of neurosurgical procedures and the low magnetic field of the open magnet system, intraoperative MRI usually results in relatively low resolution, noisy images. However, visualization during IGNS can be enhanced by preoperatively acquired data, whose acquisition and subsequent processing are

not limited by any time restriction. For example, conventional magnetic resonance images (MRI) provide high resolution anatomical information with increased spatial resolution and contrast. Functional MRI provides maps that are correlated with the activation of specific regions of the brain as certain tasks are performed. Magnetic resonance angiography (MRA) provides the locations of blood vessels, and diffusion tensor MRI (DT-MRI) provides information on the structure of the white matter by measuring the diffusion of water molecules in multiple directions. Figure 1-2 displays an example of the models that can be created from these imaging modalities.

Multi-modality registration allows pre-surgical data, including modalities that cannot currently be acquired intraoperatively such as those described above, and nuclear medicine scans such as PET and SPECT, to be visualized together with intraoperative data. Registration requires estimating, tracking, and characterizing complex shapes and motions in order to best deform the preoperative image volumes to match the intraoperative images. In such applications, physics-based deformable modeling provides an appropriate mechanism for modeling tissue properties and estimating the motion. Accurate registration results therefore depend on the quality of the model. As the brain is better represented, the results, and our confidence in them, should be improved.

The goal of this thesis was to extend a physics-based biomechanical model for non-rigid registration, designed and developed by Ferrant[6], by incorporating the underlying structure of the brain tissue to better capture changes in the brain shape as it deforms. The deformations estimated by the model were then applied to preoperatively acquired data of different modalities, including fMRI, MRA, and DT-MRI, in order to make the information provided by such data available to the surgeon during the procedure. To meet the real-time constraints of neurosurgery, Tei [38] developed a series of scripts to run Ferrant's registration algorithm, which take advantage of high performance computing. The changes to the model described in this thesis were invisible to those scripts to maintain this capability. In addition, the computation time required for assembling and solving the Finite Element Model must remain on the order of a few minutes.

1.2 Context of Work

Several image-based and physics-based matching algorithms have been developed to capture changes in image volumes across time or across subjects. Hill[14] reviews several of these methods. Those specific to IGNS and biomechanical modeling will be discussed in Chapter 2. Ferrant et al.[8] employed a biomechanical model, which treats the brain as an isotropic, linear elastic material. The approach was to use a Finite Element (FE) discretization, by constructing an unstructured grid representing the geometry of key brain structures in the intraoperative dataset, in order to model important regions while reducing the number of equations that need to be solved. The rapid execution times required by neurosurgical operations were achieved by using parallel hardware configurations, along with parallel and efficient algorithm implementations. This work extends the model to allow for anisotropy and heterogeneous elasticity parameters within each segmented structure.

The deformation of the brain is rapidly and accurately captured during neurosurgery using intraoperative images and the biomechanical registration algorithm. This model has allowed us to align preoperative data to volumetric scans of the brain acquired intraoperatively, and thus to improve intraoperative navigation by displaying brain changes in three dimensions to the surgeon during the procedure. An example of this intraoperative visualization is shown in Figure 1-3.

1.3 Contributions

Overall, the goal of this thesis is to extend the current implementation of the non-rigid registration algorithm [6] to incorporate the underlying structure of the brain tissue into the biomechanical model, while still maintaining the ability to use the results of the registration in near real-time.

The registration software [6, 38] was extended to make it possible to apply the deformation field, calculated from the volumetric deformation of the model, to DT-MRI images. Visualizations of the deformed DT-MRI and white matter structure are

Figure 1-3: Preoperative models of tumor (green), ventricles (blue), fMRI activation (aqua), blood vessels (red), and white matter tracts (yellow) on an intraoperative axial slice.

then available in addition to the MRI, MRA, fMRI volumes and models.

The linear elastic Finite Element model implementation was extended to allow for inhomogeneity and anisotropy according to the diffusion tensor data. DT-MRI provided magnitude and directional information of the diffusion of water, which has been shown to correspond to the anisotropy of brain tissue. Local elasticity parameters are calculated from the degree of anisotropy of the corresponding voxels, the direction of the anisotropy, and input material parameter estimates.

Using synthetic data to represent an elastic solid containing fibers along its length, we used diffusion information to modify the internal deformation of the solid given the

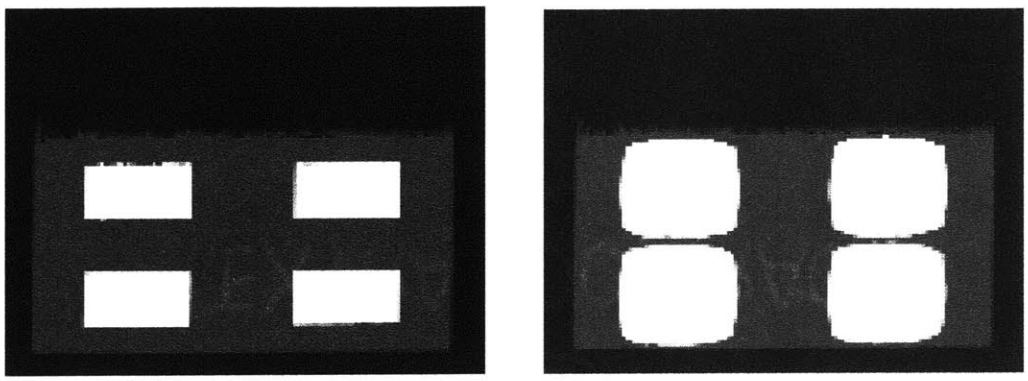

(a) After isotropic deformation (b) After anisotropic deformation

Figure 1-4: Cross-section of fiber phantom after volumetric deformation.

same surface boundary conditions. Figure 1-4 shows a cross-section of the phantom after deformation calculated by the isotropic and anisotropic models.

The registration algorithm was then applied to several surgical cases retrospectively. From the results of those cases, the elasticity parameter estimates can be optimized. Finally, the registration results were compared to those of the isotropic linear elastic model in order to evaluate the amount, if any, of improvement made by extending the model.

1.4 Organization of Thesis Document

This work presents an anisotropic, heterogeneous, linear elastic biomechanically-based method for tracking non-rigid brain deformations during IGNS procedures. The first part of the thesis (Chapter 2) describes previous related work in the field. The second part describes the preoperative image acquisition and processing, as well as the implementation details of the registration algorithm (Chapters 3 to 5). The third part presents results for synthetic data and for several neurosurgical cases (Chapter 6). The last part of this document (Chapter 7) reiterates the contributions of this thesis and describes directions for future research related to this work. The overview of each chapter follows.

Chapter 2 summarizes related work in registration for image guided neurosurgery, biomechanical modeling, and estimations of the material properties of the brain.

Chapter 3 explains the design of the Finite Element model. Also, the relationship between the DT-MRI data and the material parameters required by the model is defined.

Chapter 4 describes the acquisition of preoperative image volumes and the non-rigid registration algorithm.

Chapter 5 describes diffusion tensor MRI acquisition and its physical basis. The techniques for processing, visualization, and warping according to a known deformation are described as well.

Chapter 6 presents the verification with the synthetic data and evaluates the performance of the model in comparison with the isotropic linear elastic model.

Chapter 7 presents a discussion of the results described in this thesis. In addition, this chapter draws conclusions and provides directions for future research related to this work.

Chapter 2

Related Work

2.1 IGNS Registration Methods

In order to take advantage of image guidance during a neurosurgical procedure, diagnostic image data must be correlated to the corresponding site of pathology in the patient in physical space, which can be accomplished with localized probe tracking [16, 35]. Sets of images are then acquired at various timesteps throughout the surgery in order to track the changes that occur as the skull and dura are opened and sections of the tumor are resected. These images are typically lower resolution, and the processing and additional acquisitions that were available preoperatively are no longer practical. Therefore, in order to most effectively continue to use the preoperative images and models, accurate registration between preoperative image volumes and images that are acquired throughout the surgery is necessary.

The first issue in utilizing preoperative images in conjunction with intraoperative image sets is to correct for patient motion, which is generally limited to rotation and translation of the skull. Detection and correction of such movement errors during the acquisition of images is a basic prerequisite for accurate treatment and have therefore been a focus of much of the research in IGNS registration in order to provide a continuous update of the patient's head position during surgery. These rigid-body techniques will be described in section 2.1.1. However, clinical experience in IGNS in deep brain structures and with large resections has exposed the limitations of these

registration and visualization approaches. During neurosurgical procedures, the brain undergoes non-rigid deformations. The spatial coordinates of brain structures and adjacent lesions may change significantly. The leakage of cerebro-spinal fluid after opening the dura, the administration of anaesthetic and osmotic agents, hemorrhage, hyperventilation, and retraction and resection of tissue are all contributing factors to the deformation [7]. Figure 2-1 shows an example of brain shift during a neurosurgical case.

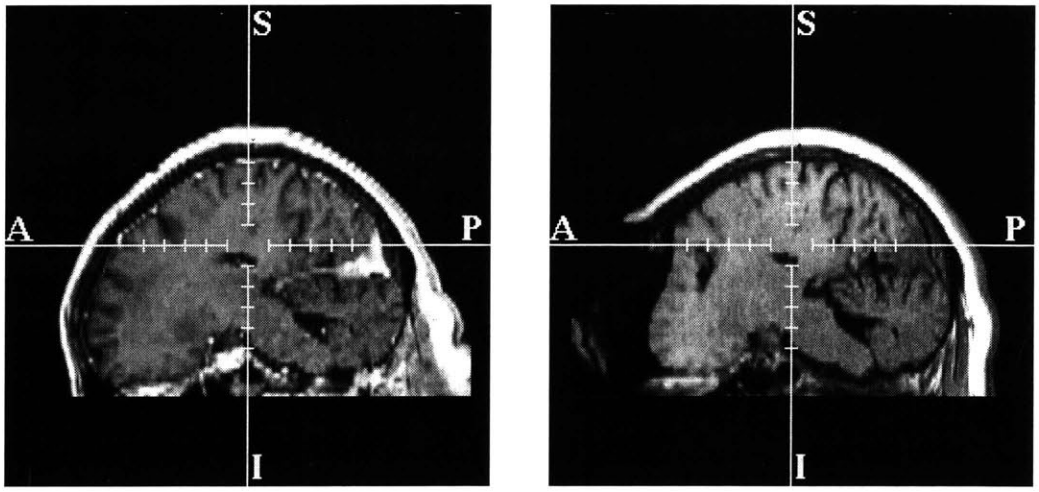

(a) Preoperative image (b) Intraoperative image

Figure 2-1: These two sagittal slices show brain shift that occurred during a neurosurgical procedure.

Samset and Hirschberg[35] found that the target shift, characterizing the motion of the region of interest, can be even more severe than the gross brain shift. This motivates the investigation of improved visualization methods and registration algorithms that can capture the non-rigid deformations the brain undergoes during neurosurgery, which will be described in section 2.1.2.

2.1.1 Marker-Based Techniques

There are a variety of methods that utilize fiducial markers in order to account for the translation and rotation of the head as the patient moves. This rigid body model

allows for extremely fast and robust calculations of the transformation, yielding near-continuous updating of the image volume according to the motion of the head.

Specifically, Lee et al. [19] present several numerical algorithms for rigid-body registration of line fiducial objects to their marks in cross-sectional planar images, such as those obtained in CT and MRI, given the correspondence between the marks and line fiducials. They provide reliable registration of incomplete fiducial patterns when up to two-thirds of the total fiducials are missing for the image, and the transformation can be calculated in as little as less than half a second. Kozak et al. [18] also register according to the locations of fiducial markers, but automate a segmentation algorithm for locating the centroid of the markers in image space. This allows for a semiautomatic registration, which they show to be an improvement in accuracy and reproducibility over manual registration. Maurer et al. [16] describe an extrinsic-point-based, interactive image-guided neurosurgical system as well. Multimodal image-to-image and image-to-physical space registration is accomplished using implantable markers. Instead of artificial markers, Westermann and Hauser [43] use feature correspondence to determine the rigid body transformation for motion correction. This provides on-line tracking of the patient's head.

These methods provide continuous, fast tracking, but depend on markers, which are typically on the exterior of the skull and limit the registration to rigid deformations. These techniques provide no information on how the brain actually deforms. To go beyond the problem of patient motion and account for the non-rigid deformation that occurs inside the skull as the surgery progresses, a second focus of research has been in developing biomechanical models to capture, and even predict, these non-rigid changes.

2.1.2 Biomechanical Models

Because there are a multitude of factors involved in the deformation of the brain, there is a wide range of models available. Most either represent the brain as some kind of elastic solid or consolidated material. Necessary parameter values are generally determined via a literature study of direct measurements, described in section 2.2.

These models are also used for comparisons to physical measurements of material parameters, development of brain atlases, and predictions of brain injury, as well as other applications. Additionally, similar models are used for other organs such as the heart.

Davatzikos [4] describes a technique based on elastically deformable models for the spatial transformation of brain images. A deformable surface algorithm is used to find a parametric representation of the outer cortical surface and then to define a map between corresponding cortical regions in two brain images. Based on the resulting map, a 3D elastic warping transformation is determined. This transformation models images as inhomogeneous elastic objects, which are deformed into registration with each other by external force fields. The elastic properties of the images can vary from one region to the other, allowing more variable brain regions, such as the ventricles, to deform more freely than less variable ones. Instead of defining a representation of corresponding cortical surfaces, Hagemann et al. [12] implement a two-dimensional case where a set of homologous landmarks must be specified, which determine correspondences. Extending the linear elastic model further, Rexilius [33] computes elasticity parameters for every voxel based on a segmentation of white matter, grey matter, cerebro-spinal fluid and background. A linear elastic model has also been implemented for the left ventricle of the heart [30]. Papademetris estimates a dense motion field using a transversely anisotropic linear elastic model, which accounts for the fiber directions in the left ventricle.

The approach of Miga et al. [25] focuses on gravity-induced deformation which results from the drainage of cerebrospinal fluid from the cranial cavity. It is based on a Finite Element rendering of consolidation physics, where the mechanics of the continuum are characterized by an instantaneous deformation at the contact area, followed by subsequent additional displacement over time as interstitial fluid drains in the direction of strain-induced pressure gradients (i.e. from high to low pressure) when subjected to load.

West et al. [42] also model tissue deformation with consolidation mechanics, but represent the brain as a porous medium where displacement is coupled to fluid

pressure. Hydraulic conductivity is defined as a scalar for each tissue element, except in areas with directional preference, in which case it is replaced by the diffusion tensor. The computed pressure field shows signs of localized disturbances which are congruent with zones having a high degree of anisotropy.

These biomechanical models are limited primarily by two factors. The most significant at the present time is the computational overhead associated with calculating a Finite Element solution for each update, which limits the complexity of the model that is practical for use in IGNS. The second is that in order to capture deformations well, some knowledge of material properties of the brain is required. Determination of these properties will be discussed in the next section.

2.2 Material Properties of the Brain

Traditionally, material parameters are measured either *in vivo* in animal studies or *in vitro* with excised animal or human brain tissue. In determining these parameters, it is important to keep in mind that there are differences across species and before and after removal of tissue. Fresh adult human brain tissue properties were found to be slightly stiffer than adult porcine properties but considerably less stiff than the human autopsy data [32]. To overcome these issues, *in vivo* measurements of human brain parameters are desired. Recently, Magnetic Resonance Elastography has been developed to provide a map of elasticity parameters, derived from MRI, across the image.

2.2.1 *In Vitro* Measurements

Miller [26] constructed a large deformation, linear, viscoelastic model and evaluated material constants based on unconfined compression experiment results on swine brain tissue. Miller and Chinzei also implemented non-linear[27] and hyper-viscoelastic[28] models and performed similar *in vitro* experiments. Their most recent model accounts well for brain tissue deformation behavior in both tension and compression for strain rates ranging over five orders of magnitude. Additionally, Morrison et al. [15] designed

and characterized an *in vitro* system capable of mechanically injuring cultured tissue at high strain rates.

These experiments did not take into account the anisotropy of brain tissue, particularly in white matter. Shuck and Advani [37] dealt with the experimental determination and analytical characterization of *in vitro* human brain dynamic constitutive properties in pure shear. Values of the storage and loss components of the dynamic shear modulus were computed and a four parameter, linear, viscoelastic model representing brain tissue properties was presented. Prange and Margulies [32] measured mechanical properties of adult porcine gray and white matter brain tissues in shear as well. Consistent with local neuroarchitecture, gray matter showed the least amount of anisotropy, and corpus callosum exhibited the greatest degree of anisotropy.

2.2.2 *In Vivo* Measurements

Miller [29] compared the previously described hyper-viscoelastic model to an *in vivo* indentation experiment. The predicted forces were about 31 percent lower than those recorded during the experiment. Because the coefficients in the model had been identified based on experimental data obtained *in vitro*, and large variability of mechanical properties of biological tissues, they considered such agreement to be very good. Numerical studies showed also that the linear, viscoelastic model of brain tissue is not appropriate for the modelling brain tissue deformation even for moderate strains.

Miga et al. [22] first presented preliminary results using a heterogeneous model with an expanding temporally located mass and show that they are capable of predicting an average total displacement to 5.7 percent in an *in vivo* porcine model. In further experiments [24], they developed and quantified the deformation characteristics of the model and investigated interstitial pressure with transient behavior in brain tissue when subjected to an acute surgical load consistent with neurosurgical events. Results demonstrated that porous-media consolidation captures the hydraulic behavior of brain tissue.

2.2.3 Magnetic Resonance Elastography

Elasticity image reconstruction in MR elastography may serve the important function of providing patient-specific material properties. One approach [23] utilizes regional image similarity as a vehicle for guiding mechanical property updates in an FEM elasticity image reconstruction framework. A similar method [39] details a Finite Element based nonlinear inversion scheme for magnetic resonance elastography.

Dynamic MR elastography is based on the visualization of propagating shear waves in harmonically excited tissue. The actual elasticity information can be reconstructed from the wave pattern by different approaches resulting in maps of wave numbers, wave speeds, or direct images of shear stiffness or shear moduli. The analysis of MRE data usually aims to convert wave images into elastograms, i.e. locally resolved images of the elastic properties of tissue. For example, Braun et al. [2] simulate a two-dimensional shear wave pattern by solving the equation for a field of coupled harmonic oscillators with spatially varying coupling and damping coefficients in the presence of an external force.

2.3 Summary

For this thesis, the first steps in extending Ferrant's biomechanical model [6] are to allow for inhomogeneous material parameters, as in [12], and to allow for anisotropy, as in [30]. The more complex models are left for future work. Because we wish to compare the results of our model to the earlier one, we start with initial estimates of elasticity parameters from [6] of $3100Pa$ for Young's modulus and 0.45 for Poisson's ratio, which are within the well accepted range for brain tissue. However, we also require a measure of the relative stiffness along and across fibers in the white matter. The studies of anisotropic brain tissue in [32, 37] are limited to *in vitro* experiments of certain regions of the brain, such as the corpus callosum, and do not link the material properties to the diffusion properties in those regions. However, it has been shown the cross-fiber direction is typically between 2x and 10x stiffer than the fiber direction, which we use as a basis of our experiments described in Chapter 6.

Chapter 3

Finite Element Modeling of Elastic Membranes and Volumes

For the biomechanical model implemented by Ferrant [6] and extended here, the brain is treated as a linear elastic solid. This chapter introduces the required elasticity theory and the framework for the Finite Element modeling of elastic volumes and surfaces.

3.1 Stress and Strain Equations

Assuming a linear elastic continuum with no initial stresses or strains, the deformation energy of an elastic body submitted to externally applied forces can be expressed as [47]:

$$E = \frac{1}{2}\int_{\Omega} \sigma^T \epsilon \, d\Omega + \int_{\Omega} \vec{F}^T \vec{u} \, d\Omega, \tag{3.1}$$

where $\vec{u} = \vec{u}(\vec{x})$ is the displacement vector, $\vec{F} = \vec{F}(\vec{x})$ the vector representing the forces applied to the elastic body (forces per unit volume, surface forces or forces concentrated at nodes), and Ω the body on which one is working. ϵ is the strain tensor:

$$\epsilon = \begin{pmatrix} \epsilon_x & \gamma_{xy} & \gamma_{zx} \\ \gamma_{xy} & \epsilon_y & \gamma_{yz} \\ \gamma_{zx} & \gamma_{yz} & \epsilon_z \end{pmatrix} \tag{3.2}$$

and σ the stress tensor:

$$\sigma = \begin{pmatrix} \sigma_x & \tau_{xy} & \tau_{zx} \\ \tau_{xy} & \sigma_y & \tau_{yz} \\ \tau_{zx} & \epsilon_{yz} & \sigma_z \end{pmatrix} \tag{3.3}$$

In the case of linear elasticity, each stress component is directly proportional to each strain component, linked by the elastic stiffnesses, $\mathbf{D}_{ijkl}$ which compose a fourth-rank tensor [13].

$$\sigma_{ij} = \sum_{k=1}^{3} \sum_{l=1}^{3} D_{ijkl} \epsilon_{kl} \tag{3.4}$$

As the above equation stands, there are 81 components in the stiffness tensor. However, because of symmetry and reciprocal relations, σ and ϵ can be represented in vector notation as:

$$\vec{\epsilon} = (\epsilon_x, \epsilon_y, \epsilon_z, \gamma_{xy}, \gamma_{yz}, \gamma_{zx})^T \tag{3.5}$$

$$\vec{\sigma} = (\sigma_x, \sigma_y, \sigma_z, \tau_{xy}, \tau_{yz}, \tau_{zx})^T . \tag{3.6}$$

Thus the stiffness tensor becomes a 6x6 symmetric matrix for a general anisotropic material (21 independent components).

$$\vec{\sigma} = \mathbf{D}\vec{\epsilon} \tag{3.7}$$

Additionally, the strain vector $\vec{\epsilon}$ now relates to the displacement $\vec{u}$ as follows:

$$\vec{\epsilon} = \left(\frac{\partial \vec{u}}{\partial x}, \frac{\partial \vec{u}}{\partial y}, \frac{\partial \vec{u}}{\partial z}, \frac{\partial \vec{u}}{\partial x} + \frac{\partial \vec{u}}{\partial y}, \frac{\partial \vec{u}}{\partial y} + \frac{\partial \vec{u}}{\partial z}, \frac{\partial \vec{u}}{\partial x} + \frac{\partial \vec{u}}{\partial z} \right) \tag{3.8}$$

$$\vec{\epsilon} = \begin{pmatrix} \frac{\partial}{\partial x} & 0 & 0 \\ 0 & \frac{\partial}{\partial y} & 0 \\ 0 & 0 & \frac{\partial}{\partial z} \\ \frac{\partial}{\partial y} & \frac{\partial}{\partial x} & 0 \\ 0 & \frac{\partial}{\partial z} & \frac{\partial}{\partial y} \\ \frac{\partial}{\partial z} & 0 & \frac{\partial}{\partial x} \end{pmatrix} \vec{u} = \mathbf{L}\vec{u} \tag{3.9}$$

In the case of an orthotropic material, the material has three mutually perpendicular planes of elastic symmetry. Hence there are three kinds of material parameters:

- the Young's moduli E_i relate tension and the stretch in the main orthogonal directions,
- the shear moduli G_{ij} relate tension and stretch in other directions than those of the planes of elastic symmetry,
- the Poisson's ratios ν_{ij} represent the ratio of the lateral contraction due to longitudinal stress in a given plane.

If the material's main orthogonal directions coincide with the coordinate axes, one has:

$$\begin{array}{lll} E_x = \frac{\partial \sigma_x}{\partial \epsilon_x} & E_y = \frac{\partial \sigma_y}{\partial \epsilon_y} & E_z = \frac{\partial \sigma_z}{\partial \epsilon_z} \\ G_{xy} = \frac{\partial \tau_{xy}}{\partial \gamma_{xy}} & G_{yz} = \frac{\partial \tau_{yz}}{\partial \gamma_{yz}} & G_{zx} = \frac{\partial \tau_{zx}}{\partial \gamma_{zx}} \\ \nu_{xy} = -\frac{\partial \epsilon_y}{\partial \epsilon_x} & \nu_{yz} = -\frac{\partial \epsilon_z}{\partial \epsilon_y} & \nu_{zx} = -\frac{\partial \epsilon_x}{\partial \epsilon_z} \end{array} \tag{3.10}$$

Thus for an orthotropic material there are nine unknown parameters. The elasticity matrix then becomes:

$$\mathbf{D} = \frac{1}{\Delta} \begin{pmatrix} \frac{1-\nu_{yz}\nu_{yz}}{E_y E_z} & \frac{\nu_{xy}+\nu_{zx}\nu_{yz}}{E_y E_z} & \frac{\nu_{zx}+\nu_{yz}\nu_{xy}}{E_y E_z} & 0 & 0 & 0 \\ \frac{\nu_{xy}+\nu_{zx}\nu_{yz}}{E_y E_z} & \frac{1-\nu_{zx}\nu_{zx}}{E_x E_z} & \frac{\nu_{yz}+\nu_{xy}\nu_{zx}}{E_y E_z} & 0 & 0 & 0 \\ \frac{\nu_{zx}+\nu_{yz}\nu_{xy}}{E_y E_z} & \frac{\nu_{yz}+\nu_{xy}\nu_{zx}}{E_y E_z} & \frac{1-\nu_{xy}\nu_{xy}}{E_x E_y} & 0 & 0 & 0 \\ 0 & 0 & 0 & G_{xy}\Delta & 0 & 0 \\ 0 & 0 & 0 & 0 & G_{yz}\Delta & 0 \\ 0 & 0 & 0 & 0 & 0 & G_{zx}\Delta \end{pmatrix} \tag{3.11}$$

where:

$$\Delta = \frac{1 - \nu_{xy}\nu_{xy} - \nu_{yz}\nu_{yz} - \nu_{zx}\nu_{zx} - \nu_{xy}\nu_{yz}\nu_{zx} - \nu_{xy}\nu_{yz}\nu_{zx}}{E_x E_y E_z} \tag{3.12}$$

In the case of a transversely isotropic material, the elastic deformation parameters in the plane orthogonal to the transverse isotropy direction do not differ. In Figure 3-1, the fiber direction f has one set of material properties and the cross fiber direction p has another.

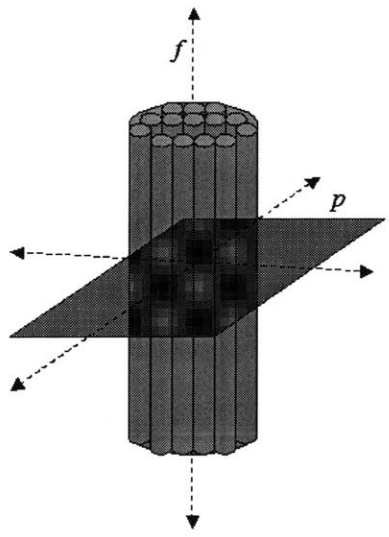

Figure 3-1: A transversely isotropic material, where the plane of isotropy p is perpendicular to the fiber direction f.

The Young's moduli, shear moduli and Poisson's ratios in plane p are identical. In this example, for transverse isotropy along the z axis, this means that $E_x = E_y = E_p$,

$G_{zx} = G_{yz} = G_f$, and $\nu_{zx} = \nu_{yz} = \nu_{fp}$. The shear modulus for the plane of isotropy is calculated from known parameters by $G_{xy} = \frac{E_p}{2(1+\nu_p)}$. The number of unknown material parameters is therefore limited to five for a transversely isotropic material to determine the elasticity matrix in Equation 3.11.

For a material with the maximum symmetry, i.e. an isotropic material, the material properties are the same in every direction. The elasticity matrix of an isotropic material then has the following symmetric form:

$$\mathbf{D} = \frac{E(1-\nu)}{(1+\nu)(1-2\nu)} \begin{pmatrix} 1 & \frac{\nu}{(1-\nu)} & \frac{\nu}{(1-\nu)} & 0 & 0 & 0 \\ \frac{\nu}{(1-\nu)} & 1 & \frac{\nu}{(1-\nu)} & 0 & 0 & 0 \\ \frac{\nu}{(1-\nu)} & \frac{\nu}{(1-\nu)} & 1 & 0 & 0 & 0 \\ 0 & 0 & 0 & \frac{1-2\nu}{2(1-\nu)} & 0 & 0 \\ 0 & 0 & 0 & 0 & \frac{1-2\nu}{2(1-\nu)} & 0 \\ 0 & 0 & 0 & 0 & 0 & \frac{1-2\nu}{2(1-\nu)} \end{pmatrix} \tag{3.13}$$

In this case, Young's modulus and Poisson's ratio are the same in any direction. There are no independent shear moduli and the total number of independent parameters is reduced to two.

3.2 Rotation of Axes

For medical applications, the material's main orthogonal directions rarely coincide with the coordinate axes. In fact, the main orthogonal directions are not even consistent across the volume. However, if the local stiffness matrix $\mathbf{D}$ in the local coordinate system is known, it is possible to calculate the rotated $\mathbf{D}$ in the global coordinate system, defined as $\mathbf{D}'$.

In this case, we assume that we can estimate the principal fiber direction and degree of anisotropy from the diffusion tensor at each voxel (see Chapter 5 for further detail). We can calculate a stiffness matrix for the transversely isotropic material, where the fiber direction is the axis of anisotropy and the cross-fiber direction de-

termines the corresponding isotropic plane. The coordinate system is defined by the eigenvectors of the diffusion tensor, sorted according to the size of the corresponding eigenvalue. Each of the eigenvectors is a column vector and forms the coordinate system matrix $\mathbf{X}$.

$$\mathbf{X} = \begin{pmatrix} \vec{x}_1 & \vec{x}_2 & \vec{x}_3 \end{pmatrix} = \begin{pmatrix} e_{11} & e_{12} & e_{13} \\ e_{21} & e_{22} & e_{23} \\ e_{31} & e_{32} & e_{33} \end{pmatrix} \tag{3.14}$$

This local stiffness matrix must then be rotated from the local coordinate system defined by the fiber direction into the global coordinate system.

Here we define the global coordinate system, $\mathbf{X}'$, in the standard way.

$$\mathbf{X}' = \begin{pmatrix} \vec{x}'_1 & \vec{x}'_2 & \vec{x}'_3 \end{pmatrix} = \begin{pmatrix} \vec{x} & \vec{y} & \vec{z} \end{pmatrix} = \begin{pmatrix} 1 & 0 & 0 \\ 0 & 1 & 0 \\ 0 & 0 & 1 \end{pmatrix} \tag{3.15}$$

The directional cosine matrix defined in [13] determines the transformation.

$$\mathbf{A} = \begin{pmatrix} \cos(\vec{x}'_1, \vec{x}_1) & \cos(\vec{x}'_1, \vec{x}_2) & \cos(\vec{x}'_1, \vec{x}_3) \\ \cos(\vec{x}'_2, \vec{x}_1) & \cos(\vec{x}'_2, \vec{x}_2) & \cos(\vec{x}'_2, \vec{x}_3) \\ \cos(\vec{x}'_3, \vec{x}_1) & \cos(\vec{x}'_3, \vec{x}_2) & \cos(\vec{x}'_3, \vec{x}_3) \end{pmatrix} \tag{3.16}$$

Substituting in our values for $\mathbf{X}$ and $\mathbf{X}'$, the transformation matrix is simply $\mathbf{X}$. Returning to the earlier notation, the transformation is applied to the fourth-rank stiffness tensor.

$$\mathbf{D}'_{ijkl} = \sum_{m=1}^{3} \sum_{n=1}^{3} \sum_{o=1}^{3} \sum_{p=1}^{3} A_{im} A_{jn} A_{ko} A_{lp} \mathbf{D}_{mnop} \tag{3.17}$$

However, this can be simplified with the vector notation [47] to:

$$\mathbf{D}' = \mathbf{T}\mathbf{D}\mathbf{T}^{\mathbf{T}} \tag{3.18}$$

where

$$\mathbf{T} = \begin{pmatrix} e_{11}^2 & e_{21}^2 & e_{31}^2 & 2e_{21}e_{11} & 2e_{31}e_{21} & 2e_{31}e_{11} \\ e_{12}^2 & e_{22}^2 & e_{32}^2 & 2e_{22}e_{12} & 2e_{32}e_{22} & 2e_{32}e_{12} \\ e_{13}^2 & e_{23}^2 & e_{33}^2 & 2e_{23}e_{13} & 2e_{33}e_{23} & 2e_{33}e_{13} \\ e_{11}e_{12} & e_{21}e_{22} & e_{31}e_{32} & e_{21}e_{12} + e_{11}e_{22} & e_{31}e_{22} + e_{21}e_{32} & e_{31}e_{12} + e_{11}e_{32} \\ e_{12}e_{13} & e_{22}e_{23} & e_{32}e_{33} & e_{22}e_{13} + e_{12}e_{23} & e_{32}e_{23} + e_{22}e_{33} & e_{32}e_{13} + e_{12}e_{33} \\ e_{11}e_{13} & e_{21}e_{23} & e_{31}e_{33} & e_{21}e_{13} + e_{11}e_{23} & e_{31}e_{23} + e_{21}e_{33} & e_{31}e_{13} + e_{11}e_{33} \end{pmatrix} \tag{3.19}$$

3.3 Finite Element Framework

Equation 3.1 is valid whether one is working with a surface or a volume. We model our active surfaces, which represent the boundaries of the objects in the image, as elastic membranes, and the surrounding and inner volumes as 3D volumetric elastic bodies.

Within a finite element discretization framework, an elastic body is approximated as an assembly of discrete finite elements interconnected at nodal points on the element boundaries. This means that the volumes to be modeled need to be meshed, i.e. divided into elements. Our volumetric and surface meshing algorithms will be described in Chapter 4.

The continuous displacement field $\mathbf{u}$ within each element is approximated as a function of the displacement at the element's nodal points $\mathbf{u}_i^{el}$ weighted by its shape functions $N_i^{el} = N_i^{el}(\mathbf{x})$.

$$\mathbf{u} = \sum_{i=1}^{N_{nodes}} N_i^{el} \mathbf{u}_i^{el} \tag{3.20}$$

The elements we use are tetrahedra (number of nodes per element $N_{nodes} = 4$) for the volumes and triangles for the membranes ($N_{nodes} = 3$), with linear interpolation of the displacement field. Hence, the shape function of node i of element el is defined as:

$$N_i^{el} = K\left(a_i^{el} + b_i^{el}x + c_i^{el}y + d_i^{el}z\right) \tag{3.21}$$

where $K = \frac{1}{6V^{el}}$ for a tetrahedron, and $K = \frac{1}{2S^{el}}$ for a triangle. The computation of V^{el}, S^{el} and the interpolation coefficients is detailed by [47].

The discretization of the domain allows us to solve for displacements only at the location of the discretization nodes of the domain. The displacement within each element is linked to the nodal displacements through its associated shape functions. Through such a discretization, and because the integral over the whole domain can be seen as the sum of the integrals over every element, it is possible to evaluate the equilibrium equations separately on every element, and to sum up the contribution of every triangle to which a vertex is connected to build a global equilibrium matrix system.

For every node i of each element el, we define the matrix $\mathbf{B}_i^{el} = \mathbf{L}_i N_i^{el}$. The function to be minimized on each element el can thus be expressed as

$$E\left(\mathbf{u}_i^{el}, \cdots, \mathbf{u}_{N_{nodes}}^{el}\right) = \frac{1}{2}\int_\Omega \sum_{i=1}^{N_{nodes}} \sum_{j=1}^{N_{nodes}} \mathbf{u}_i^{el^T} \mathbf{B}_i^{el^T} \mathbf{D} \mathbf{B}_j^{el} \mathbf{u}_j^{el}\, d\Omega + \int_\Omega \sum_{i=1}^{N_{nodes}} \mathbf{F} N_i^{el} \mathbf{u}_i^{el}\, d\Omega \tag{3.22}$$

We seek the minimum of this function by solving for

$$\frac{\partial E\left(\mathbf{u}_i^{el}, \cdots, \mathbf{u}_{N_{nodes}}^{el}\right)}{\partial \mathbf{u}_i^{el}} = 0 \quad ; \qquad i = 1, \cdots, N_{nodes} \tag{3.23}$$

The earlier equation then becomes:

$$\int_\Omega \sum_{j=1}^{N_{nodes}} \mathbf{B}_i^{el^T} \mathbf{D} \mathbf{B}_j^{el} \mathbf{u}_j^{el}\, d\Omega = -\int_\Omega \mathbf{F} N_i^{el}\, d\Omega \quad ; \qquad i = 1, \cdots, N_{nodes} \tag{3.24}$$

This last expression can be written as a matrix system for each finite element:

$$\mathbf{K}^{el}\mathbf{u}^{el} = -\mathbf{F}^{el} \tag{3.25}$$

Matrices $\mathbf{K}^{el}$ and vector $\mathbf{F}^{el}$ are defined as follows.

$$\mathbf{K}_{i,j}^{el} = \int_{\Omega} \mathbf{B}_i^{elT} \mathbf{D} \mathbf{B}_j^{el} \, d\Omega \mathbf{F}_i^{el} = \int_{\Omega} \mathbf{F} N_i^{el} \, d\Omega \tag{3.26}$$

where every element i, j refers to pairs of nodes of the element el. $\mathbf{K}_{i,j}^{el}$ is a 3x3 matrix, and $\mathbf{F}_i^{el}$ is a 3x1 vector. The 12x12 matrix $\mathbf{K}^{el}$, and the vector $\mathbf{F}^{el}$ are computed for each element. The coefficients i, j of the local matrices are summed up at the locations $g(i), g(j)$ in the global matrix (where $g(i)$ represents the number of the element's node in the entire mesh). The assembly of the local matrices then leads to a global system

$$\mathbf{K}\mathbf{u} = -\mathbf{F}, \tag{3.27}$$

the solution of which will provide us with the deformation field corresponding to the global minimum of the total deformation energy.

We now have constitutive equations that model surfaces as elastic membranes and volumes as elastic bodies. Given externally applied forces $\mathbf{F}$ to a discretized body characterized by a rigidity matrix $\mathbf{K}$, solving the previous equation provides us with the resulting displacements.

The resulting displacements can then be used to characterize the deformation the brain has undergone during the course of surgery using the stress and strain tensors. Using shape functions, stress and strain tensors can be derived from the displacement field at every nodal point i, given every tetrahedron of the FE model to which the node belongs, and using the following relationships:

$$\epsilon_i = \mathbf{L}_i N_i \mathbf{u}_i \tag{3.28}$$

$$\sigma_i = \sum_{el|i \in el} \mathbf{D} \mathbf{L}_i N_i^{el} \mathbf{u}_i \tag{3.29}$$

Chapter 4

Non-Rigid Registration Algorithm

4.1 Methodology Overview

The steps, both pre- and intra-procedural, of the registration method used for this thesis can be summarized as follows:

1. **Preoperative image acquisition, processing and visualization**: Before the surgery, a conventional grey-scale MRI scan, functional MRI, MRA, and DT-MRI datasets are acquired. These images are processed to locate key structures, such as regions of cortical activation, blood vessels, and white matter tracts. They are then manually registered to the grey-scale MRI by the neurosurgeon. For the segmentations required for registration, a binary curvature driven evolution algorithm [46], which deforms contours according to a coupled set of curve equations, is used to extract the surfaces of the brain and ventricles. 3D Slicer [10], an integrated software tool allowing for the display of all this data simultaneously, is used for visualization and surgical planning. A sample preoperative view is shown in Figure 4-2 and other details of the acquisition and processing are described in Section 4.2.

2. **Intraoperative image acquisition**: The open configuration MR scanner is used to acquire intraoperative scans 3-5 times throughout the procedure, as necessary. Section 4.3.1 lists the parameters for the image acquisitions and

shows an example intraoperative image.

3. **Intraoperative segmentation**: The segmentation technique for the brain and ventricles described above is performed on each of the acquired intraoperative images.

4. **Intraoperative rigid registration**: The presurgical data is registered to the intraoperative patient scan using an automated, Mutual Information-based algorithm [40, 21] that optimizes the rotations about the three axes and the translations along them. Section 4.3.3 explains the registration algorithm further and shows an example of the result of the rigid registration.

5. **Intraoperative non-rigid registration**: An active surface matching method deforms the preoperative surface meshes of the brain and ventricles to the corresponding segmentations of the intraoperative target. The resulting surface displacements serve as boundary conditions to the biomechanical model, which solves for the volumetric deformation. The deformation field is then applied to the data acquired preoperatively. Algorithm details and deformation field images are included in Section 4.3.3.

6. **Intraoperative visualization**: The matched preoperative data is visualized using 3D Slicer. Section 4.3.4 provides an example of preoperative data mapped onto an intraoperative slice and explains how the visualization is combined with the optical tracking system.

4.2 Preoperative Steps

4.2.1 Image acquisition

Before surgery, an MRI examination is performed using a 1.5-Tesla clinical scanner (Signa Horizon; GE Medical Systems, Milwaukee, WI). The standard protocol at the Brigham and Women's Hospital for IGNS cases includes the acquisition of the following:

- A T1-weighted, spoiled gradient echo (SPGR) volume (124 1.5mm thick sagittal slices, TR=35msec, TE=5msec, Flip Angle=45, FOV=24cm, matrix=256x192, NEX=1),
- A T2-weighted fast spin echo (FSE) volume (124 sagittal slices, TR=600msec, TE=19msec, FOV=22cm, matrix=256x192, NEX=1),
- A phase-contrast MR angiograph (PC-MRA, 60 sagittal slices, TR=32msec, Flip Angle=20, FOV=24 cm, matrix= 256x128, NEX=1),
- An fMRI exam (HORIZON EPIBOLD sequence, 21 contiguous 7mm coronal slices, TE=50msec, TR=3sec, FOV=24cm, matrix=64x64, 6 alternating 30-seconds epochs of stimulus and control tasks), given to patients whose pathology is located within the vicinity of the motor cortex.
- A DT-MRI scan (TR=2.4s, TE=65msec, b_{high}=1000s/mm^2, b_{low}=5s/mm^2, FOV=24cm, slice thickness=4mm, gap=1mm)

4.2.2 Processing

Segmentation

For the purposes of registration, the SPGR patient scan is segmented using a binary curvature driven evolution algorithm, as described by Yezzi et al. in [46]. It is a region-based approach to snakes designed to optimally separate the values of certain image statistics over a known number of region types. Multiple sets of contours deform according to a coupled set of curve evolution equations derived from a single global cost functional. The coupling between evolution equations, which does not depend upon the mutual proximities of each set of contours, causes every single pixel in the image to influence the flow of every indvidual contour. This fully global approach to segmentation is therefore robust to initial contour placement. It takes only a few seconds to select a threshold and to click inside of the region to be segmented, but it requires manual correction of misclassified skin and muscle. This procedure is utilized to obtain a segmentation of both the brain and the lateral ventricles of the subject.

Meshing

Medical images are represented by an array of a finite number of image samples, or voxels. These could be used as discretizing elements of a Finite Element model; however, to limit computational complexity, it is desirable to work with fewer elements. This implies that many elements will cover multiple image samples. Each element should represent image samples that can be treated in the same way in the model, such as those of a single tissue type. For computational ease and because they provide better representations of the domains, triangular elements are chosen to represent surfaces and tetrahedral elements to represent volumes.

A tetrahedral mesh generator, specifically suited for meshing anatomical structures using 3D labeled images, has been developed by Ferrant [6]. This approach combines volume tetrahedralization and recursive mesh subdivision.

An initial multi-resolution, octree-like tetrahedral approximation of the volume to be meshed is computed depending on the underlying image content. Next, an isovolume tetrahedralization is computed on the initial multi-resolution tetrahedralization, such that it accurately represents the boundary surfaces of the objects depicted in the image.

The algorithm first subdivides the image into cubes of a given size, which determine the resolution of the coarsest tetrahedra in the resulting mesh. The cubes are then tetrahedralized, and at locations where the mesh needs better resolution to follow the boundary surfaces, the tetrahedra are further divided adaptively into smaller tetrahedra, yielding an octree-like mesh. This subdivision causes cracks for tetrahedra that are adjacent to subdivided tetrahedra. In this case the neighboring tetrahedra are remeshed using a precomputed case table. The resulting mesh contains pyramids and prisms, which are further tetrahedralized. Finally, the labels of the vertices of each tetrahedron are checked in a marching tetrahedra fashion. If the tetrahedron lies across the boundary of two objects with a different label, it is subdivided along the edges on the image's boundary so as to have an exact representation of the boundary between the objects. The resulting mesh contains prisms, which are

further tetrahedralized. The surface meshes for an example surgical case are shown in Figure 4-1.

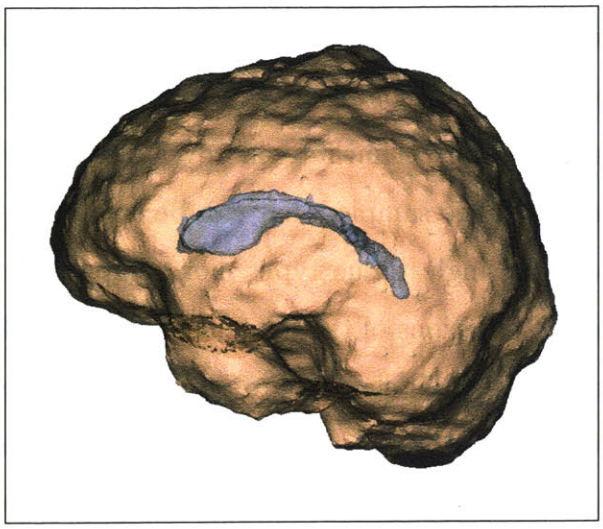

Figure 4-1: The meshes resulting from segmenting the brain and lateral ventricles.

4.2.3 Visualization for Surgical Planning

We chose to use the 3D Slicer(*http://www.slicer.org*), developed mainly by Gering and O'Donnell [10], an integrated surgical guidance and visualizations system which provides capabilities for data analysis and on-line interventional guidance. The 3D Slicer allows for the display of intraoperative images along with preoperative data. This system is the platform of choice for IGNS procedures in the MRT room, providing the visualization of virtual surgical instruments in the coordinate system of the patient and patient image acquisitions. The images we constructed were presented on the LCD monitor in the MRT operating room to increase the information available to the surgeon as the operation progresses.

In the surgical planning stage, all preoperative datasets have been manually registered by the neurosurgeon to match the preoperative SPGR volume. An array of information derived from fusing these multi-modality datasets containing information on morphology (MRI, MRA, DT-MRI), cortical function (fMRI), and metabolic activity (PET/SPECT) can be visualized simultaneously. Additionally, the segmentations of the brain and ventricles created for the registration algorithm and other

segmentations of key structures including the skin, tumor, arteries, veins, etc. can be superimposed on the gray-scale images. Tractography derived from DT-MRI, explained in greater detail in Chapter 5, displays the locations of white matter tracts. Models are combined in a 3D scene in Figure 4-2.

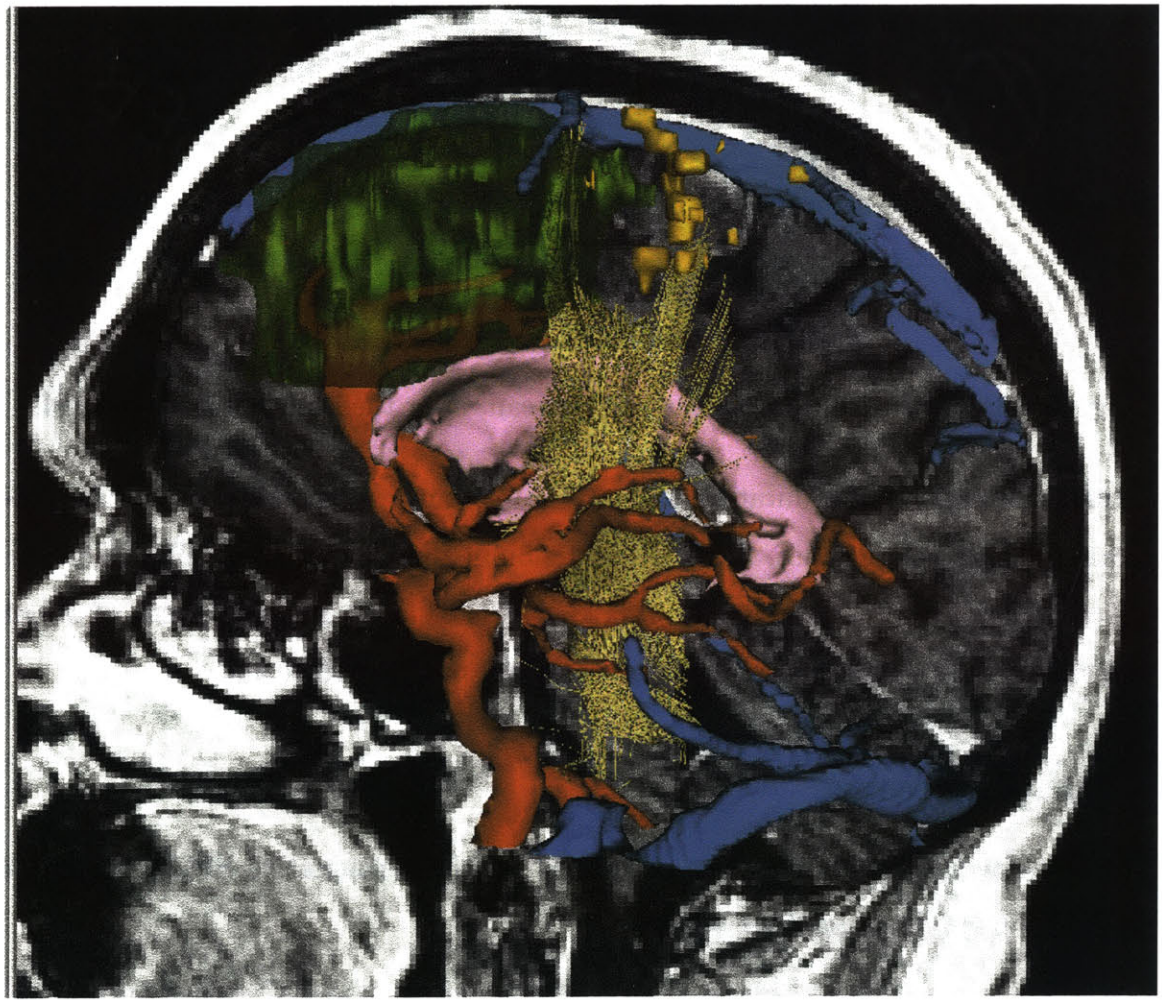

Figure 4-2: A sagittal slice with the arteries (red), veins(blue), ventricles (lavender), fMRI activation (gold), white matter tracts (yellow), and tumor (green)superimposed.

4.3 Intraoperative Steps

4.3.1 Image acquisition

MRI scans are acquired intraoperatively through an open-configuration MR system (Signa SP; GE Medical Systems, Milwaukee, WI). These images are collected 3 to

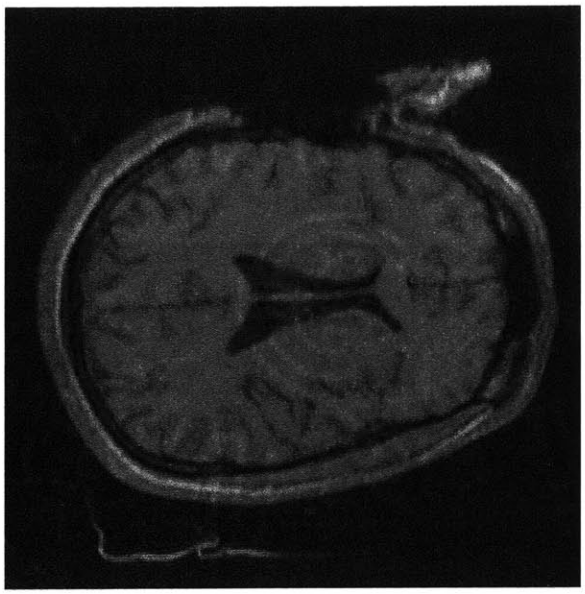

Figure 4-3: Axial slice from intraoperative scan, after the skull has been opened.

5 times throughout the duration of every craniotomy, as necessitated by the procedure. These volumes are 3D SPGR (60 2.5mm thick axial slices, TR=28.6msec, TE=12.8msec, FOV=24, matrix=256x128, NEX=1), with imaging times of about four minutes. A sample intraoperative image is shown in Figure 4-3.

4.3.2 Processing

The same segmentation that was performed on the preoperative SPGR volume is repeated on the intraoperative volume.

4.3.3 Registration

Rigid Registration

For rigid registration of the preoperative SPGR volume to the intraoperative SPGR, a Mutual Information based registration algorithm, introduced by Wells et al. [40] and Maes and Collignon [21], is used. The rotations about each of the axes and translations along each of the axes, for a total of six parameters, are optimized using the Powell method with Mutual Information as the cost function. The rigidly registered and resampled preoperative image is shown in Figure 4-4(b).

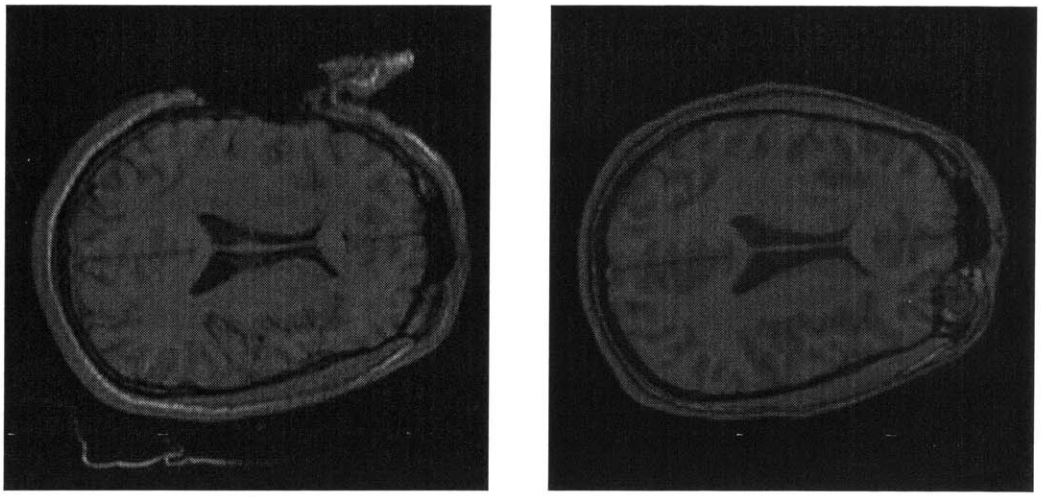

(a) Intraoperative Image

(b) Rigidly Registered Preoperative Image

Figure 4-4: Sagittal slice from the preoperative volume rigidly registered to the intraoperative volume.

Active Surface Deformation

We model our active surfaces, which represent the boundaries of the objects in the image, as elastic membranes, and the surrounding and inner volumes as 3D volumetric elastic bodies, as described in Chapter 3. Within a finite element discretization framework, an elastic body is approximated as an assembly of discrete finite elements interconnected at nodal points on the element boundaries. The equations modeling elastic membranes presented in Chapter 3 can be used to solve tracking problems in 3D images by means of deformable surface models. An active contour is characterized by three parts [6]:

- *internal forces* – elasticity and bending moments describing the contour as a physical object, designed to hold the curve together, and locally smooth (first order terms) as well as keeping it from bending too much (second order terms);
- *external forces* – forces describing how the active contour is attracted to the desired features of the image data;

- *iterative procedure* – process which attempts to find the configuration that best matches both the internal and external forces.

The 2D active contour model has been extended to 3D surfaces by Cohen and Cohen [3], who also proposed to discretize the resolution of the equations governing the behavior of the surfaces using finite elements. In this way, the iterative variation of the surface can be discretized using finite differences, provided the time step τ is small enough. Image-derived forces $\mathbf{F}^{\mathbf{v}^t}$ (forces computed using the surface's nodal position $\mathbf{v}$ at iteration t) are applied to the active surface to deform it. The constitutive equation for elastic membranes for the active surface yields the following iterative equation:

$$\frac{\mathbf{v}^t - \mathbf{v}^{t-1}}{\tau} + \mathbf{K}\mathbf{v}^t = -\mathbf{F}^{\mathbf{v}^{t-1}}, \tag{4.1}$$

which can be written as:

$$(\mathbf{I} + \tau\mathbf{K})\mathbf{v}^t = \mathbf{v}^{t-1} - \tau\mathbf{F}^{\mathbf{v}^{t-1}}. \tag{4.2}$$

The external forces driving the elastic membrane towards the edges of the image structure are integrated over each element of the mesh and distributed over the nodes belonging to the element using its shape functions. The image force $\mathbf{F}$ is computed as a decreasing function of the gradient such that it is minimized at the edges of the image. For correct convergence, the surfaces need to be initialized very close to the edges of the object to which they need to be matched. Prior information about the surface to be matched gives an initial global repositioning of the surface and can be very useful to account for global shape changes such as rescaling and rotation. The distance measure can be efficiently computed by precomputing the distance from any pixel to the reference surface using the Distance Transform algorithm described by Ferrant [6]. Such a transform provides a good initialization for running an active surface algorithm next that can then account for local shape changes of the surface.

Ferrant [6] increased the robustness and the convergence rate of the surface deformation by computing the forces as a gradient descent on a distance map of the edges

in the target image. The external force can be described by the following expression:

$$\mathbf{F}(\mathbf{x}) = S_{min} G_{exp} \nabla(\mathcal{D}(I(\mathbf{x}))), \tag{4.3}$$

where $\mathcal{D}(I(\mathbf{x}))$ represents the distance transformation of the target image at point $\mathbf{x}$. S_{min} is chosen so that the gradient points towards a point with a smaller distance value, while G_{exp} is the contribution of the expected gradient sign on the labeled image.

Biomechanical Volumetric Deformation

A model developed by Ferrant [6], and extended here to further incorporate the object's physical characteristics, has been implemented to improve the accuracy of the deformable registration.

An algorithm for doing elastic image matching using a finite element discretization was developed, with the idea of modifying the constitutive equation of volumetric bodies described in the previous chapter to incorporate the image similarity constraint into the expression of the potential energy of an elastic body submitted to external forces. The elastic potential energy then serves as a physics-based regularity constraint to the image similarity term. The full details of the mathematical formulation of the volumetric elastic image matching using the FE method are found in Chapter 3.

The implementation of this method for doing physics-based registration of images uses boundary deformation of the important structures to infer a volumetric deformation field. The algorithm presented in the previous section was used to track the deformation of boundary surfaces of key objects and that deformation was used as input to a volumetric FE elastic model. The approach yields a deformation field satisfying the constitutive equations of the body, and can be used to characterize the deformation the body has undergone from the initial to the target image. A sagittal slice of the deformation fields for the displacement in x, y, and z are shown in Figure 4-5.

(a) x displacement (b) y displacement (c) z displacement

Figure 4-5: Sagittal slice of the deformation fields calculated by the biomechanical model.

Volumetric Deformation Field Application

Finally, the volumetric deformation fields are applied to the preoperative image datasets. The warped grey-scale image is shown in Figure 4-6(b). Such deformed data can then be visualized using an integrated visualization system as described in the next section.

A new deformation field is calculated and applied to the previously matched data on each new intraoperative scan. In this manner, successive scans can be matched during the neurosurgical procedure. The entire method, including segmentation, rigid and deformable registration (when implemented as a linear elastic model), is usually completed in less than 12 minutes [38].

4.3.4 Intraoperative Visualization

Applying the non-rigid deformation algorithm to the preoperative data allows the visualization described in Section 4.2.3 to provide updated, reliable information during IGNS procedures. An example result is shown in Figure 4-7. The scene presented to the surgeon consists not only of models of critical brain structures, but also of reformatted slices that are driven by a tracked surgical device. The location of the imaging plane is specified with an optical tracking system (Flashpoint; Image Guided Technologies, Boulder, CO). The spatial relationship (position and orientation) of this system relative to the scanner is reported with an update rate of 10Hz. A visual-

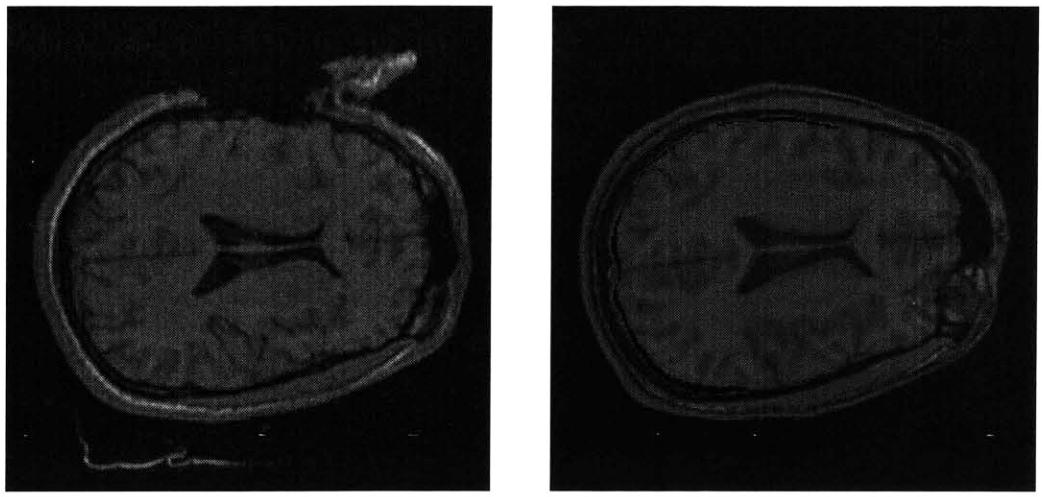

(a) Intraoperative Image (b) Warped Preoperative Image

Figure 4-6: Sagittal slice from the preoperative volume warped to match the intraoperative volume.

ization workstation (Ultra 30; Sun Microsystems, Mountain View, CAB) is connected to the MR scanner with a TCP/IP network connection and contains two Sun Creator 3D graphics accelerator cards. One drives the 20-inch display in the control area of the surgical suite, and the other outputs the 3D view to color LCD panels in the scanner gantry.

Whenever the position and orientation of the optical tracking system change, or a new image is acquired, a server process sends the new data to the 3D Slicer software resident on the visualization workstation. In this way, surface models, are visualized together with the tracked surgical instrument. Thus, presurgical data, non-rigidly aligned to intraoperative images, augments interventional imaging to expedite tissue characterization and precise localization and targeting.

4.4 Summary

In this chapter, the registration algorithm was presented. First, the grey-scale MRI, fMRI, MRA, and DT-MRI datasets are acquired preoperatively for processing, visualization, and surgical planning. After an automatic rigid registration to the intra-

operative volume, the brain and ventricles are segmented from the grey-scale MRI. Using these segmentations, tetrahedral meshes are generated for the brain and ventricles. The corresponding surfaces are deformed to match the intraoperative target segmentations. Those surface displacements serve as boundary conditions to the Finite Element model, which solves for the displacements at each node of the preoperative volumetric mesh. Finally, the deformation field calculated by the FEM is applied to each of the preoperative datasets for intraoperative visualization.

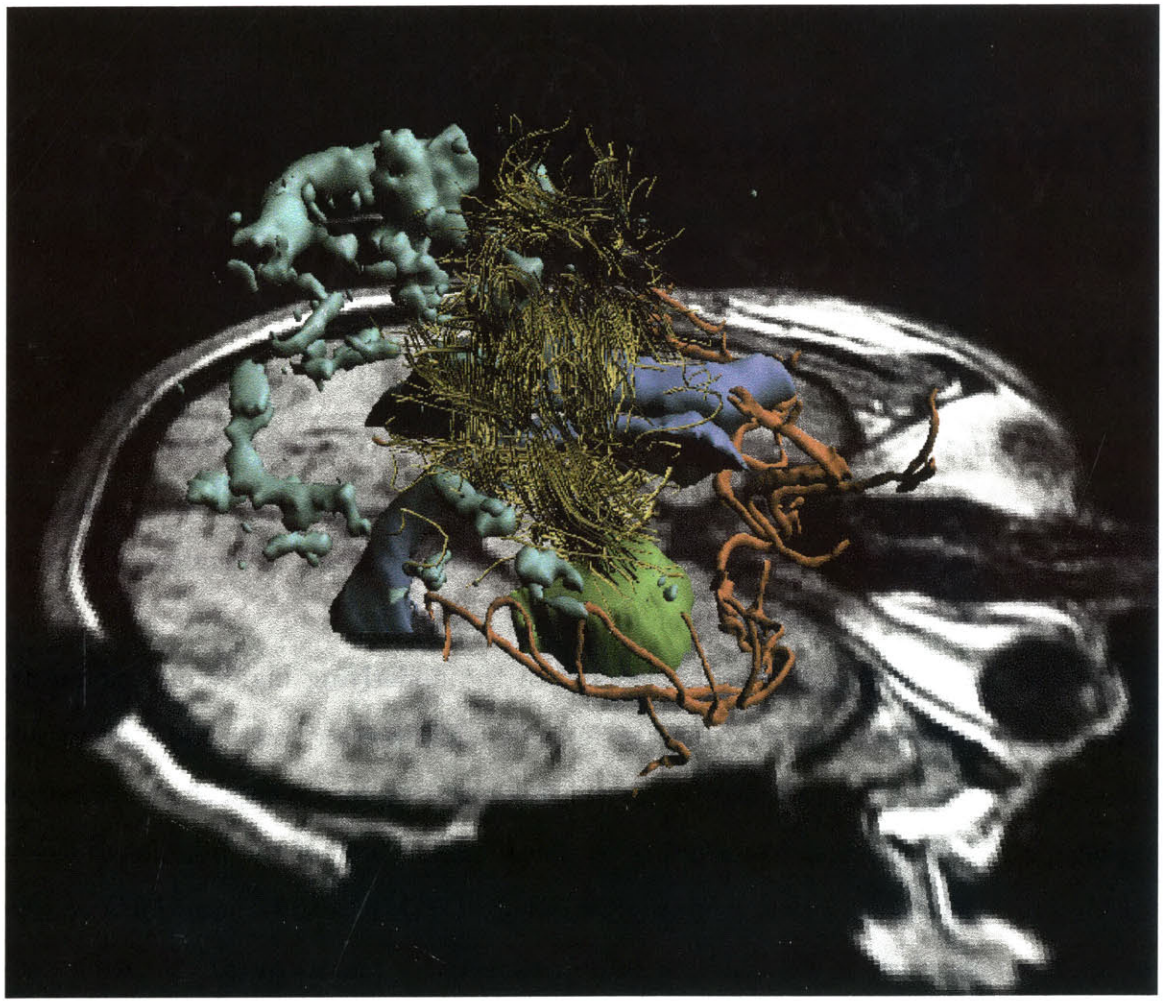

Figure 4-7: An intraoperative axial slice with the blood vessels (red), ventricles (blue), fMRI activation (gold), white matter tracts (yellow), and tumor (green) superimposed.

Chapter 5

Diffusion Tensor MRI

5.1 Background

Diffusion Tensor MRI (DT-MRI) is a technique developed to allow non-invasive quantification of diffusion of water *in vivo*. The directional dependence of water diffusion rates can be closely related to the anisotropy of the structure. Therefore, DT-MRI can be used to infer the organization of tissue components.

In the brain, high anisotropy reflects both the underlying highly directional arrangement of white matter fiber bundles forming white matter tracts and their intrinsic microstructure. This anisotropy can be characterized to distinguish the principal orientation of diffusion, corresponding to the dominant axis of the bundles of axons making up white matter tracts in an given voxel. DT-MRI can be used for a variety of applications, such as determining brain connectivity measures [31], locating neuronal fiber pathways [5, 20], identifying relationships between functional activation patterns and structural properties of brain pathways [41], quantifying anisotropy in brain tissue types [9, 36], and modeling the behavior of other organs, such as the heart [34].

For the work in this thesis, non-rigid registration results depend on the representation of the brain by the biomechanical model. Because different histologic types of brain white matter demonstrate significant and reproducible anisotropy differences [36], it would be expected that they would deform differently and thus should be mod-

eled differently. DT-MRI can provide information on this structure to be incorporated into the model.

5.2 Image Acquisition

The diffusion tensor is measured by sensitizing the MRI signal intensity to the random motion of water. The acquisition and processing techniques used for all the DT-MRI data described in this work were implemented by Westin et al. [44] and are described briefly below.

The imaging uses two strong gradient pulses, symmetrically positioned around a 180° refocusing pulse, allowing for controlled diffusion weighting. The first gradient pulse induces a phase shift for all spins; the second gradient pulse inverts this phase shift, thus canceling the phase shift for static spins. Spins having completed a change of location due to Brownian Motion during the time period will experience different phase shifts by the two gradient pulses, which means they are not completely refocused and consequently will result in signal loss. For an anisotropic material, the relationship between the diffusion weighted image S and the non-diffusion weighted, but otherwise identical, image S_0 is:

$$S = S_0 \exp^{-\gamma^2\delta^2[\Delta-(\delta/3)]\mathbf{g}^\mathbf{T}\mathbf{D}\mathbf{g}} \tag{5.1}$$

where γ is the proton gyromagnetic ratio (42 MHz/Tesla), $|\mathbf{g}|$ is the strength of the diffusion sensitizing gradient pulses, δ is the duration of the diffusion gradient pulses, and Δ is the duration of the diffusion gradient pulses.

In the typical case, the symmetric 3x3 diffusion tensor $\mathbf{D}$ has six degrees of freedom. To estimate the tensor, a minimum of six measurements of S, taken from different non-collinear gradient directions, are needed in addition to the baseline image data S_0. Thus for each slice in the data set, seven images need to be collected with different diffusion weightings and gradient directions. The resulting diffusion tensor is a matrix of coefficients describing the diffusion of water molecules:

$$\mathbf{D} = \begin{pmatrix} d_{11} & d_{12} & d_{13} \\ d_{12} & d_{22} & d_{23} \\ d_{13} & d_{23} & d_{33} \end{pmatrix} \tag{5.2}$$

Diagonalization of $\mathbf{D}$ gives three pairs of eigenvalues and mutually orthogonal eigenvectors. Since molecular diffusion is hindered by encounters with cell membranes and cytoskeletal structures, the water diffusion rate parallel to a fiber is higher than perpendicular to it. The eigenvector corresponding to the largest eigenvalue (the principle eigenvector) is therefore parallel to the local tangent of a fiber.

5.3 Visualization

Visualization of DT-MRI is especially challenging because each voxel has an associated tensor instead of a scalar grey-scale or label value. There are variety of techniques, such as displaying ellipsoids with their axes corresponding to the eigenvectors and their scalings along the axes as the eigenvalues, volume renderings where opacity, color and shading are determined from the tensor information [17], planes spanned by the major and medium eigenvectors [45] and other color scheme-based methods derived from shape measures [44]. The 3D Slicer's tensor module, developed by O'Donnell, was used for all visualization of DT-MRI data for the work in this thesis, as well as during the procedures in the MRT.

5.3.1 Tensor Glyphs

The tensor module displays glyphs overlayed on the grey-scale image, where the length of the glyph corresponds to the largest eigenvalue, the direction corresponds to the principle eigenvector, and the color corresponds to the degree of anisotropy. A sample image is shown in Figure 5-1.

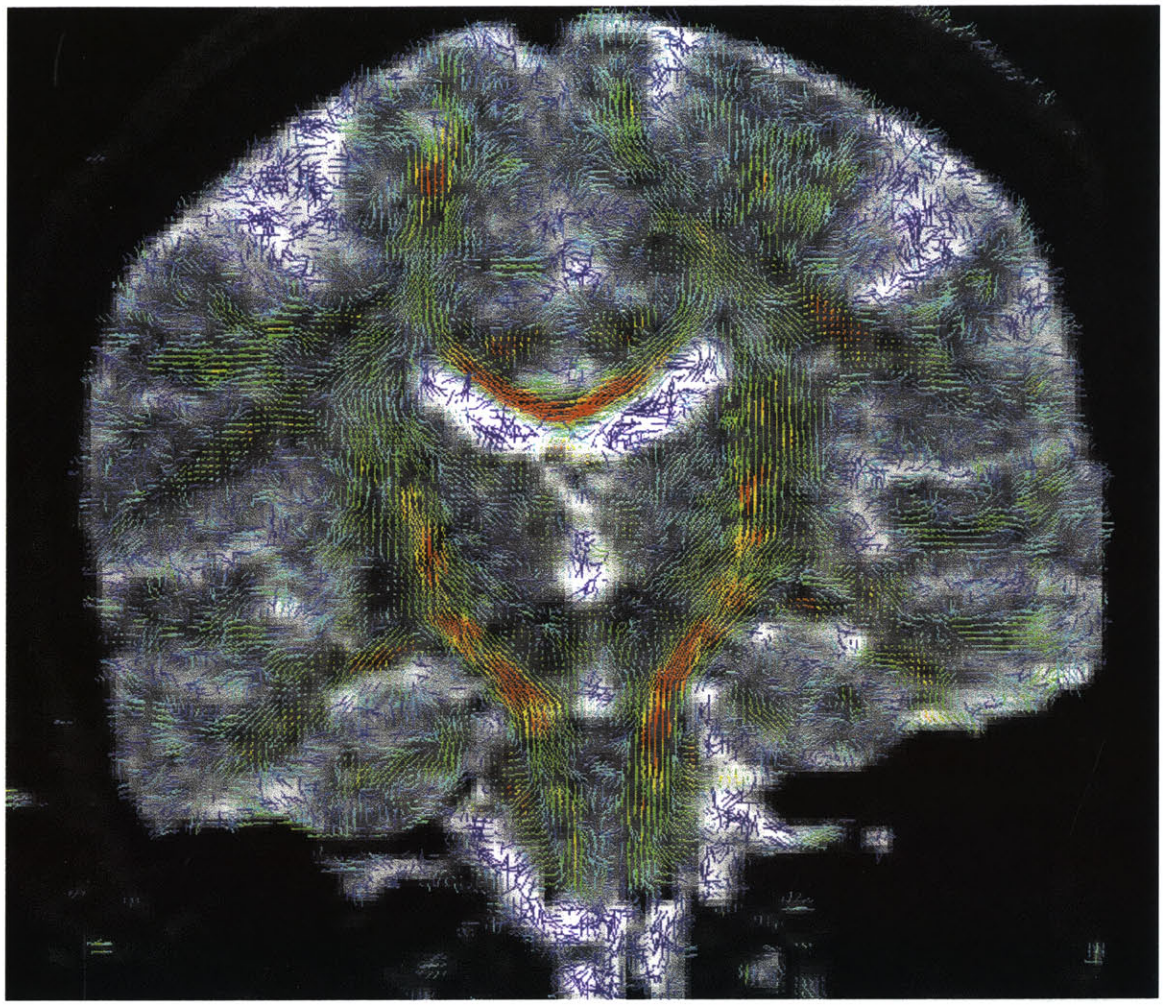

Figure 5-1: Visualization of tensor data as 3D glyphs corresponding the magnitude and direction of the diffusion tensor at each voxel. Regions of high anisotropy, such as the corpus callosum and the corticospinal tract, are in red.

5.3.2 Tractography

Additionally, DT-MRI tractography [44], which is useful for the demonstration of neural connectivity, is available. Given a starting seed point, a path of a set length is drawn along the principle eigenvector. The endpoint of that path then becomes the new seed point for the continuation of the path. These tracts, as shown in Figure 5-2 provide useful information for surgical planning.

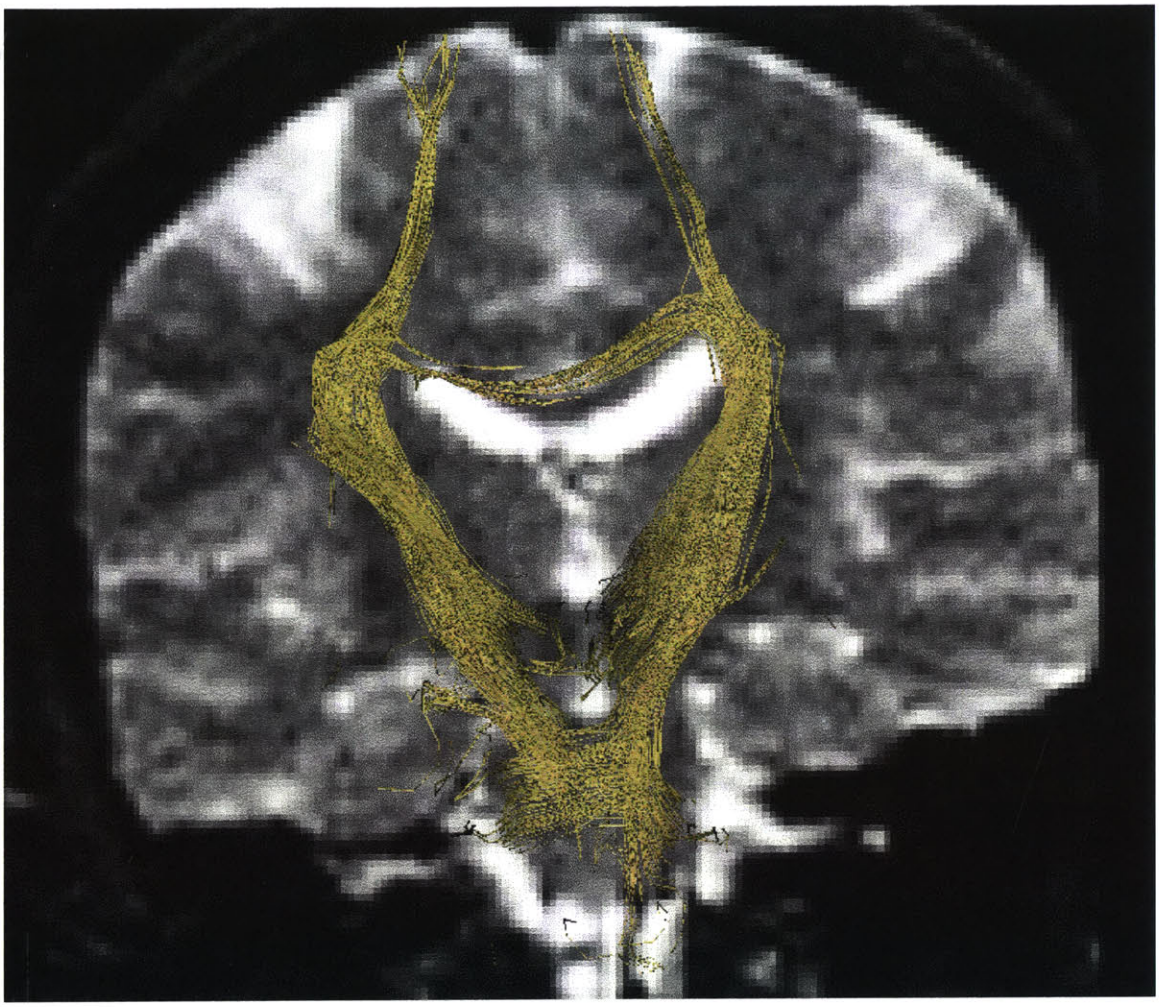

Figure 5-2: Estimated locations of example white matter tracts derived from DT-MRI.

5.4 Spatial Transformations of Tensor Volumes

5.4.1 Motivation

Deforming an initial image to match a target image via registration requires a spatial transformation to be applied. For scalar volumes, it is possible to simply copy the value at each voxel in the transformed image from the corresponding position in the original image, given some kind of interpolation method. However, if this same technique were applied to a tensor volume, such as the one in Figure 5-3(a), it would yield the result in Figure 5-3(b). The lines within the pathways of the corpus callosum no longer point along the pathway, as they did in the original image.

(a) Tensor glyph image (zoomed in around the corpus callosum)

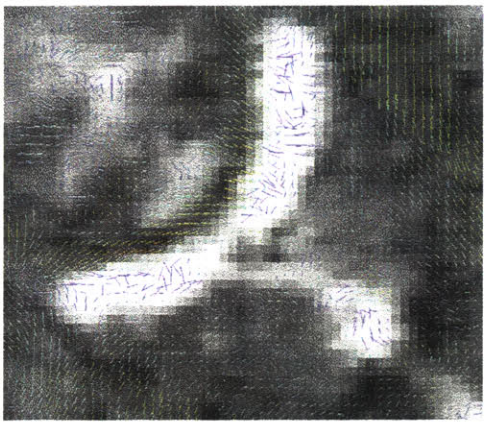

(b) Rotated image without reorientation of tensors

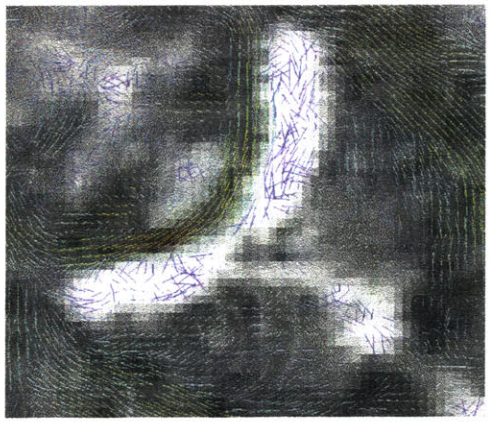

(c) Rotated image after reorientation of tensors

Figure 5-3: A 45° rotation of the DT-MRI image, with and without tensor reorientation.

Clearly the diffusion tensors themselves need to be rotated, and this can be achieved by applying the same rigid rotation matrix to each tensor in the image as was applied to the volume. If $\mathbf{R}$ is the rotation matrix representing the image transformation, $\mathbf{D}$ must be replaced by $\mathbf{D}'$:

$$\mathbf{D}' = \mathbf{R}\mathbf{D}\mathbf{R}^{\mathbf{T}} \tag{5.3}$$

For a rigid transformation the same, known, $\mathbf{R}$ is applied to each voxel, and the result is in Figure 5-3(c). This additional level of complexity can be avoided when transformation invariant tensor characteristics are registered in place of the actual tensor volume [11]. Unfortunately, the tractography and glyphs can only be visualized from the full tensor volume.

Because our registration algorithm allows non-rigid deformations, we need to extend the method to cope with higher order transformations. The first step is considering the problem of applying affine transformations, which include a deformation component that can change the shape of image regions. The size and shape of the diffusion tensors in the image should be preserved, since these are properties of the tissue microstructure, but must be reoriented in a way consistent with the reorientation of the anatomy caused by the transformations. A rigid rotation matrix, $\mathbf{R}$, at each point in the image, which reflects the local reorientation that occurs as a consequence of an affine transformation, $\mathbf{F}$, must be calculated.

5.4.2 Method

Alexander et al. [1] address the problem of applying spatial transformations to DT-MRI volumes. They present two possible methods for finding such a rotation and discuss their relative merits. One method, referred to as the *finite strain* (FS) reorientation strategy, decomposes the transformation into a rigid rotation and a pure deformation operation and uses the rigid rotation component for reorientation. A drawback of the FS reorientation strategy is that the deformation component is discarded and does not contribute to the estimated reorientation. This component

includes shearing and non-uniform scaling, which also affect the orientation of the underlying image structure, but in a more complex way than rigid rotation.

The other method, called the *preservation of principle direction* (PPD) is a reorientation strategy that takes into account and compensates for the additional reorientation caused by the deformation. In synthetic data sets, the PPD method was shown to be an effective reorientation strategy and eliminated the problems associated with FS. However, in the intra-subject human study, both methods were shown to be effective.

In the work presented in this thesis, the spatial transformations are defined by the deformation of the volumetric meshes corresponding to the structures in the brain. Although there is expected to be some orientation change that cannot be captured by the FS method, its accuracy is adequate when taking into account the limited computation time available under time constraints of the surgery.

We therefore chose to implement the *finite strain* (FS) reorientation strategy. We extract the rigid rotation component from $\mathbf{F}$ and use it to reorient each diffusion tensor in the image. Any non-singular $\mathbf{F}$ can be decomposed into a rigid rotation component, $\mathbf{R}$, and a pure deformation component, $\mathbf{U}$:

$$\mathbf{F} = \mathbf{UR}, \qquad \mathbf{R} = \mathbf{F}(\mathbf{F}^{\mathbf{T}}\mathbf{F})^{-\frac{1}{2}} \tag{5.4}$$

We generalize the method to higher order deformations by taking advantage of the local affine transformation that initial and deformed volumetric meshes provide. Every voxel in the volume that is displaced, and thus requires reorientation, is contained in one tetrahedral cell of the mesh. Each node in that mesh is displaced as the mesh is deformed by the biomechanical model. Therefore, the 3 locations of the four nodes of the tetrahedron fully determine the affine transformation that tetrahedron, and each of the voxels contained in it, undergoes. Where $\mathbf{A}$ represents the x, y, and z coordinates of each node of a given tetradron as follows:

$$\mathbf{A} = \begin{pmatrix} x_1 & y_1 & z_1 \\ x_2 & y_2 & z_2 \\ x_3 & y_3 & z_3 \\ x_4 & y_4 & z_4 \end{pmatrix} \tag{5.5}$$

the affine transform is defined as:

$$\mathbf{F} = \mathbf{A}_{\mathbf{initial}}^{-\mathbf{1}}\mathbf{A}_{\mathbf{target}} \tag{5.6}$$

R is then extracted from **F** and applied to each voxel contained in the given tetrahedron. This is then repeated for all the tetrahedra in the mesh.

5.4.3 Sample Result

In Figure 5-4, the DT-MRI volume has been deformed to match an intraoperative image where brain shift has occurred. The surface of the DT-MRI volume matches reasonably well with the intraoperative greyscale, and the tensor glyphs are aligned with the brain structures. Each of the glyphs are oriented in an expected way, consistent with the directions of the fiber structure that is present.

5.5 DTI-MRI and Material Parameters

To incorporate the white matter structure into the biomechanical model described in Chapter 3, at each tetrahedron, the local coordinate system aligned with the fiber direction and its corresponding elasticity parameters must be defined to calculate the stiffness matrix. We do this by assigning a diffusion tensor to each tetrahedron in the volumetric mesh and calculating its eigenvectors and eigenvalues. The local x direction is defined by the eigenvector with the smallest eigenvalue, the y direction by the eigenvector with the middle eigenvalue, and the z direction by the eigenvector with the largest eigenvalue (the fiber direction). The transformation matrix to the global coordinate system is calculated from these eigenvectors.

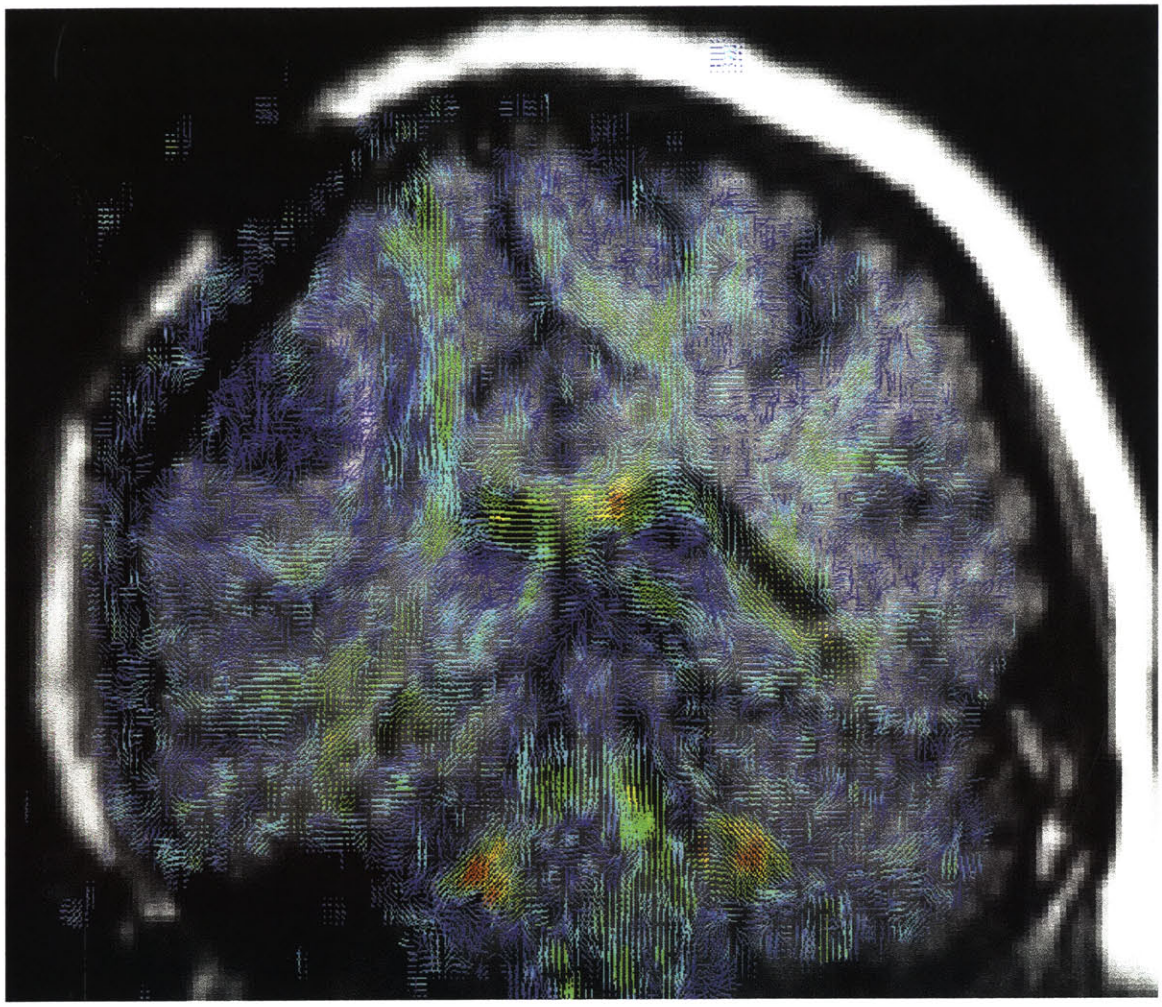

Figure 5-4: Result of deforming DT-MRI volume to an intraoperative image where the tumor has been resected and brain shift has occurred.

The stiffness matrix for a transversely isotropic material from Section 3.1 requires 5 independent parameters. From the work described in Section 2.2, the cross-fiber stiffness is approximately 2x to 10x greater than the fiber stiffness for anisotropic brain tissue. However, not all brain tissue is anisotropic. Fractional anisotropy, defined in the equation below, is calculated from the eigenvalues of the diffusion tensor and provides a quantitative measure of the degree of anisotropy of the tissue.

$$\mathbf{FA} = \frac{1}{\sqrt{2}} \frac{\sqrt{(\lambda_1 - \lambda_2)^2 + (\lambda_1 - \lambda_2)^2 + (\lambda_1 - \lambda_2)^2}}{\sqrt{\lambda_1^2 + \lambda_2^2 + \lambda_3^2}} \tag{5.7}$$

When fractional anisotropy is zero, the region is isotropic and the Young's moduli

should be the same in all three directions. When fractional anisotropy is one, the region is completely anisotropic and the Young's modulus in the cross-fiber direction should be greater than the Young's modulus in the fiber direction. Therefore, we simply calculate the Young's modulus in the cross-fiber direction as a linear function of the fractional anisotropy and maximum stiffness ratio (α) and leave the Young's modulus in the fiber direction at its default value.

$$E_p = (1 + (\alpha - 1)FA)E \qquad E_f = E \tag{5.8}$$

The Poisson's ratios are assumed to be equal in all three directions because the compressibility of the tissue is not expected to change. The shear moduli are calculated from the Young's moduli and Poisson's ratios as follows:

$$G_f = G_p = \frac{E_p}{2(1+\nu)} \tag{5.9}$$

G_f is actually an independent parameter, but it is arbitrarily set equal to the shear modulus in the plane of isotropy because the experiments for the elasticity parameters for anisotropic brain tissue focus do not include the shear moduli.

Once the local stiffness matrix has been determined, it is rotated according to the transformation matrix. The Finite Element model is then assembled just as it was in the isotropic case.

Chapter 6

Registration Results

Image-guided neurosurgery requires the most accurate registration possible within the time constraints of the procedure. It is within this context that we evaluate the performance of the registration algorithm described in Chapter 4. First, for verification of the model, we apply the algorithm to a synthetic dataset representing an elastic solid with fibers running along its length. Next, the algorithm is applied retrospectively to three surgical cases. These results include estimation of the elasticity parameters and comparison of both accuracy and time to the original isotropic model developed by Ferrant [6].

6.1 Fiber Phantom Experiment

In this experiment, the aim is to deform a linear elastic solid, containing fibers along its length, to approximately half its original height. 3D models derived from the surface of the solid and the boundaries of the fiber are shown in Figure 6-1.

To set the surface boundary conditions for the models, the surface of the phantom is matched to a target surface of the desired size and shape. For the isotropic model, the elasticity parameters are set to $\nu = 0.2$ and $E = 10000Pa$, and the displacements at each tetrahedron in the volumetric mesh are calculated by solving the Finite Element model. Because the material properties are uniform for the entire volume, the phantom is expected to deform evenly. Figure 6-2(a) shows that the

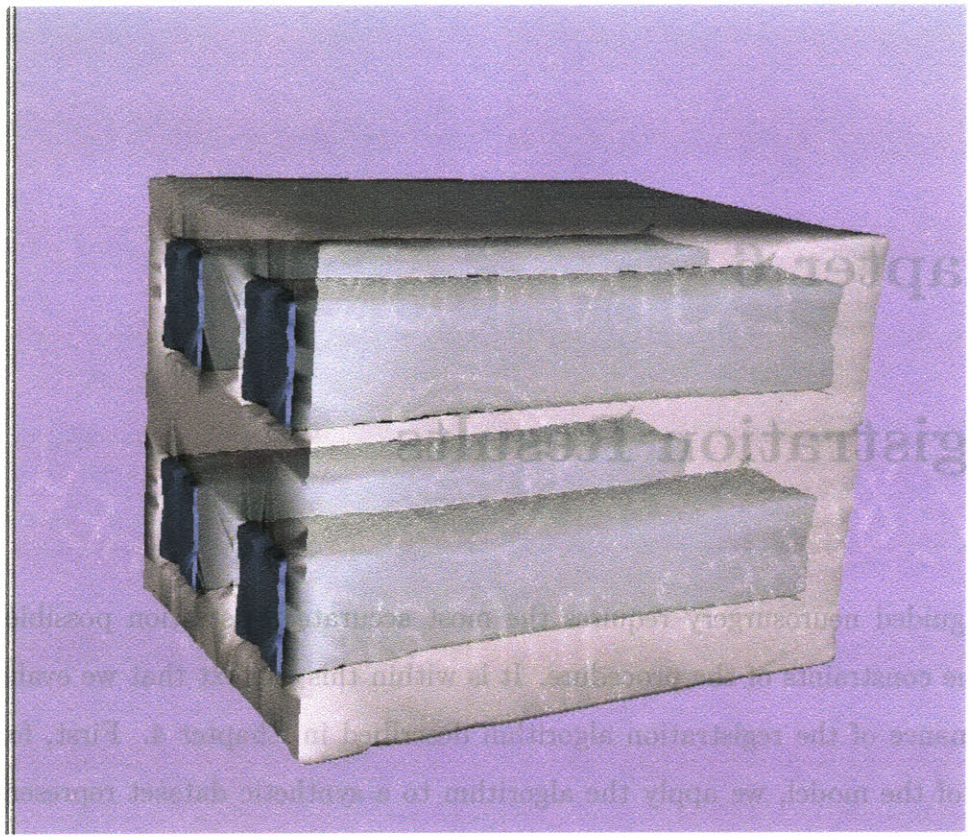

Figure 6-1: Volume rendering of the rectangular solid, containing four fibers along its length.

cross-sectional area of the fibers, as well as that of the surrounding non-fiber regions, has been decreased by approximately a factor of two.

If, however, we are to treat the synthetic fibers as if they were fiber tracts in the brain, the Young's modulus in the cross-fiber direction is larger than Young's modulus in the fiber direction in completely anisotropic regions. In order to provide this structural information to the model, a synthetic diffusion tensor MRI volume is required. For this example, we set diffusion in the non-fiber regions of the phantom to be isotropic and of relatively small magnitude. In the fibers, diffusion along the fiber direction was set at 10x greater than in the cross-fiber direction and in the isotropic regions. The glyphs representing the major eigenvectors are overlayed on a cross-section of the phantom in Figure 6-3. The equations in Section 5.5, defining how DT-MRI data relates to the elasticity parameters, therefore yield a fractional anisotropy (FA) value of 0.89 in the fibers and a Young's modulus of $9010Pa$ in the

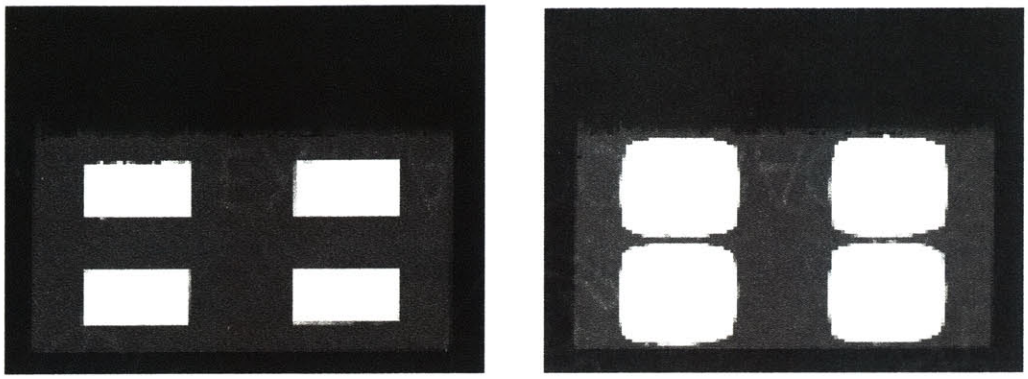

(a) After isotropic deformation (b) After anisotropic deformation

Figure 6-2: Cross-section of fiber phantom after volumetric deformation

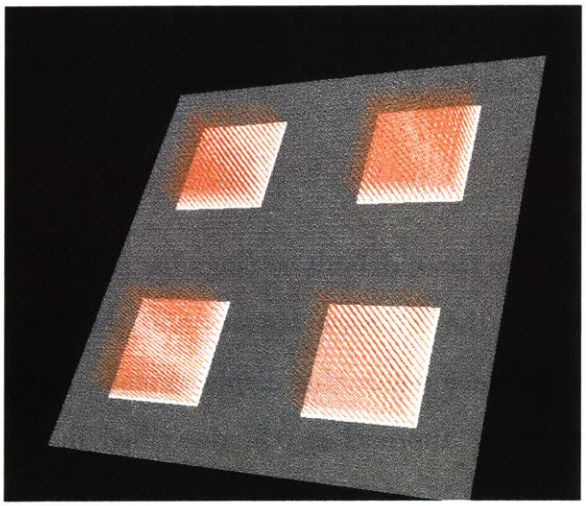

Figure 6-3: Cross-section of fiber phantom, where tensor glyphs show the preferential diffusion of water along the fibers.

cross-fiber direction when we assume that the maximum stiffness ratio is 10.

Because of the differing material properties of the fiber and the surrounding regions, we expect that the fiber will maintain its structure. This is exactly what we see in Figure 6-2(b), as the fibers have nearly the same cross-sectional area as they did in the original volume. We have shown that given the diffusion tensor at every tetrahedron in the mesh, we can calculate the local stiffness parameters at each location and automatically adjust the deformation to behave in a way consistent with what we know of the structure.

6.2 Retrospective Surgical Cases

For the surgical cases in which DT-MRI data was acquired, the volumetric deformation can be applied using both the isotropic and anisotropic linear elastic models.

6.2.1 Estimating Elasticity Parameters

The aim in this section is to determine the input elasticity parameters E and ν for both models in order to compare them consistently in later experiments. In the original implementation of this registration algorithm [6], the Young's moduli were set to $E = 3000Pa$ for the brain and $1000Pa$ for the ventricles. Poisson's ratio was set to 0.45 for both. A more detailed description of how these material properties are determined is found in Chapter 2.

Poisson's Ratio

Unfortunately, when we use those default settings for E and ν in the anisotropic case (adjusting E according to the diffusion tensors and the stiffness ratio), the Finite Element solver fails to produce reasonable displacements, likely because of numerical instabilities that occur as ν approaches 0.5, described in [6]. Therefore, we vary Poisson's ratio from 0.2 to 0.45 in Table 6.1 to determine where a solution can be found.

	$\nu = 0.20$	$\nu = 0.25$	$\nu = 0.30$	$\nu = 0.35$	$\nu = 0.42$
$\nu = 0.25$	0.259 mm				
$\nu = 0.30$	0.590 mm	0.094 mm			
$\nu = 0.35$	1.033 mm	0.227 mm	0.594 mm		
$\nu = 0.42$	11.01 mm	11.01 mm	11.00 mm	11.00 mm	
$\nu = 0.45$	220.1 mm	220.2 mm	220.2 mm	218.3 mm	215.9 mm

Table 6.1: Maximum difference in displacement fields generated with varying Poisson's ratios.

For $\nu > 0.35$, the solution does not satisfy the boundary conditions determined by the surface displacements. For $\nu < 0.35$, the boundary conditions are satisfied

and the interior deformations differ in an expected way. Repeating this experiment with the isotropic model, the maximum difference in the displacement fields when $\nu = 0.35$ (on the low end of the range of values for Poisson's ratio found in previous experiments) and when $\nu = 0.45$, is 1.24 mm. While this amount is not insignificant, it is small enough that it appears reasonable to use $\nu = 0.35$ to be able to compare the isotropic and anisotropic models consistently.

Stiffness Ratio

Determining the relative stiffness along and across the fiber is a much more challenging problem. As explained in Chapter 2, the experiments which determine the relative stiffnesses are extremely limited. The first issue is that they are *in vitro* studies, which have been show to differ considerably from *in vivo* and model results. Second, the measurements of fiber stiffnesses are in very specific regions of the brain, such as the corpus callosum and corona radiata, and the stiffness ratios differ throughout the entire brain. Next, there is no measure of how the stiffness ratio relates to anisotropy of diffusion. Finally, there is a large range of potential stiffness ratios, generally from 2x to 10x greater in the cross-fiber direction. For the most part, as was explained in Section 5.5, we calculate the relative stiffness as a linear function of the the fractional anisotropy and the maximum stiffness ratio (α) of the tissue.

To evaluate the performance of the registration algorithm by varying the maximum stiffness ratio, we use a set of landmarks identified by a neurosurgeon in both the preoperative and intraoperative image for one surgical case. These landmarks include the medial tumor margin, 3 points on the lateral temporal lobe surface, and the optic tract. In Table 6.2, the maximum stiffness ratio yields the following results for the average landmark displacement error.

From these results, we see that a maximum fiber stiffness ratio of 10 yielded the best registration given this small set of landmarks. There was no solution found by the numerical solver for $\alpha = 12$ that satisfied the surface boundary conditions, so greater ratios were ignored. For the remainder of the experiments, α is set to 10.

Maximum stiffness ratio	Average Error
$\alpha = 2$	2.7806 mm
$\alpha = 4$	2.7748 mm
$\alpha = 6$	2.7695 mm
$\alpha = 8$	2.7650 mm
$\alpha = 10$	2.7613 mm
$\alpha = 12$	no solution

Table 6.2: Max. stiffness ratio α and the displacement error averaged over the 5 landmarks.

6.2.2 Comparison to Isotropic Model

For each of the three surgical cases, both the isotropic and anisotropic models were used to deform the volumes given the same initial surface displacement boundary conditions.

Landmark Displacement Error

Using the same set of landmarks described in the previous section, we compared the registration errors of both the isotropic and anisotropic models, as well as the original rigid registration. These results are presented in Table 6.3.

Landmark Location	Rigid Reg.	Isotropic	Anisotropic
Medial Tumor Margin	1.000 mm	0.357 mm	0.357 mm
Lateral Temporal Lobe Surface (1)	7.211 mm	7.343 mm	7.143 mm
Lateral Temporal Lobe Surface (2)	2.236 mm	1.510 mm	1.512 mm
Lateral Temporal Lobe Surface (3)	2.236 mm	2.584 mm	2.559 mm
Optic Tract	2.236 mm	2.236 mm	2.236 mm
Average Error	2.984 mm	2.806 mm	2.761 mm

Table 6.3: Comparison of error in landmark displacement for rigid registration, the isotropic model, and the isotropic model.

These displacement errors are all very close, and there is a limited number of landmarks, but it appears that the anisotropic model does show a minimal amount of improvement. However, to better characterize how the isotropic and anisotropic

models differ throughout the volume, we consider the entire deformation fields in the next section.

Deformation Fields

The most direct way to compare how the volumes are deformed differently is to look for differences in the deformation fields. In Figure 6-4(a), an axial slice shows the differences in the two deformation fields. Regions of greater displacement appear brighter in the image. The regions that are bright in the image, particularly surrounding the ventricle, correspond to regions of high anisotropy. Coronal and sagittal slices are shown as well.

Axial slices from the other two surgical cases are shown in Figure 6-5. They show similar trends, with most of the changes occurring in regions of high anisotropy, but because no inter-subject registration was applied and the deformation that occurred intraoperatively was different for each surgical case, they are obviously not identical.

For a quantitative analysis of the differences in the deformation fields, Table 6.2.2 shows the maximum displacement difference in each of the three axes, the maximum displacement difference, the mean displacement difference, and the percentage of the maximum displacement.

	dx_{max}	dy_{max}	dz_{max}	D_{max}	D_{mean}	$D_{\%}$
Case 1	1.06 mm	1.30 mm	2.60 mm	2.92 mm	0.174 mm	22.6%
Case 2	0.36 mm	0.56 mm	1.14 mm	1.14 mm	0.141 mm	10.7%
Case 3	0.51 mm	0.54 mm	2.08 mm	2.08 mm	0.152 mm	24.5%

Table 6.4: Differences in deformation fields between the anisotropic and isotropic models.

Computation Time Analysis

The time constraints of a neurosurgical procedure require consideration of the additional computation time required to assemble and solve the more complex model. For the purpose of this experiment, we focus only on the assembly and solution time

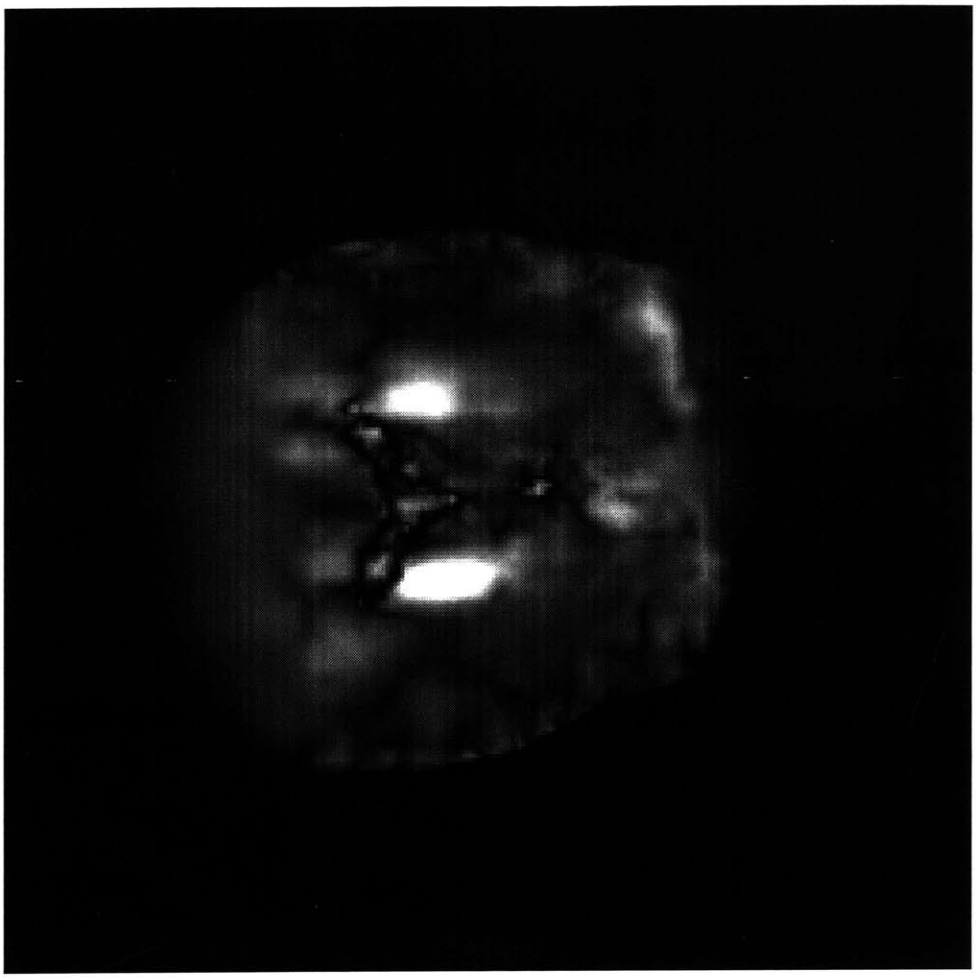

(a) Axial

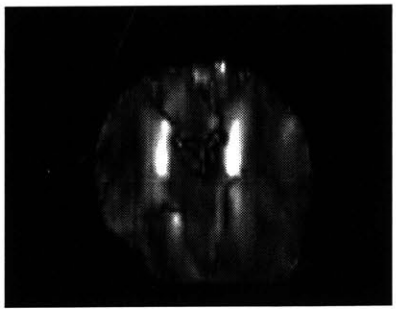

(b) Coronal

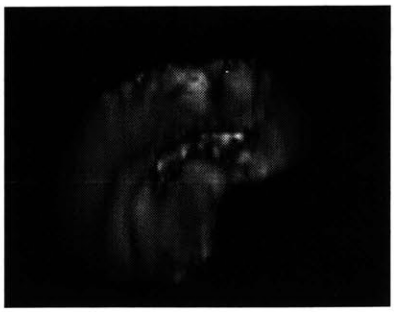

(c) Sagittal

Figure 6-4: Image representing the magnitude of the difference in displacement in the three directions (surgical case 3).

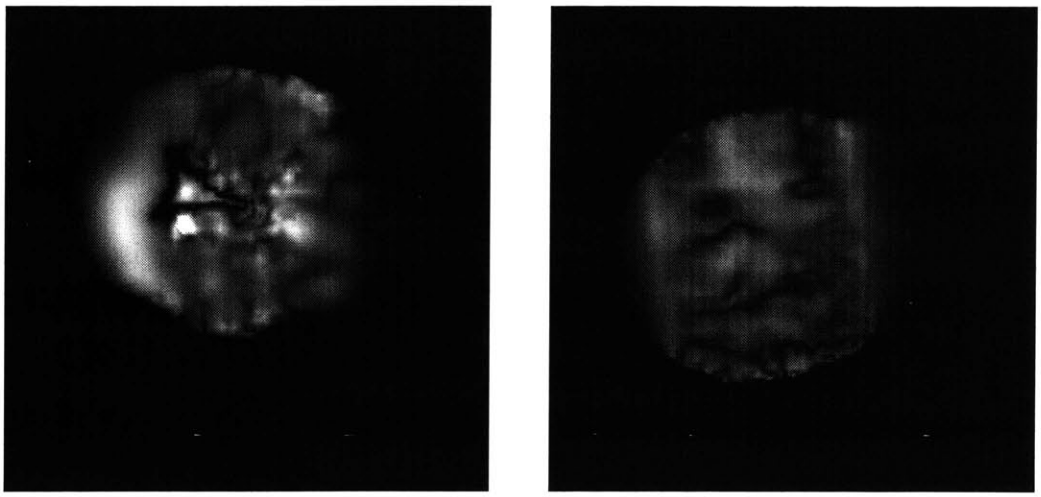

(a) Case 1 (b) Case 2

Figure 6-5: Sagittal slices of the magnitude of the difference in displacement fields for two surgical cases. Note there is no intra-subject registration used here, so the slices do not correspond.

because the additional time required (approximately 9 minutes) for segmentation, rigid registration, applying deformation fields, etc. has already been accounted for by [38].

Two major factors determine the time required for the Finite Element model. The first is the size and connectivity of the mesh, which affects both the isotropic and anisotropic computation times. The second is the amount of DT-MRI data available for the mesh. At each point where a diffusion tensor corresponding to a tetrahedron exists, the eigenvectors and eigenvalues, fractional anisotropy, and transformation matrix must be calculated. Table 6.2.2 shows that in general, the anisotropic model requires about twice as long as the isotropic one to be assembled and solved. However, this only increases the time required from 12 minutes to 14 minutes, which is still very reasonable, especially considering the rapid increases in computational power.

	Isotropic Model	Anisotropic Model
Case 1	65.6 sec	118.1 sec
Case 2	87.7 sec	175.1 sec
Case 3	97.9 sec	188.3 sec

Table 6.5: Computation time comparison between anisotropic and isotropic models.

6.3 Summary

In this chapter, we have shown that we can use DT-MRI data to incorporate structural information into the biomechanical model originally developed by Ferrant [6]. We verified that a fiber phantom will deform differently internally when the diffusion tensor is used to calculate the local elasticity parameters. The default elasticity parameters, including the Young's modulus, the Poisson's ratio, and the maximum stiffness ratio, were optimized for the anisotropic model given a limited set of landmarks identified by a neurosurgeon. The errors in landmark displacements and differences in deformation fields were compared for the isotropic and anisotropic models to evaluate registration accuracy. Finally, the computation time requirements for both models were analyzed.

Chapter 7

Conclusions

7.1 Discussion of Results

In the previous chapter, we verified that we could in fact integrate structural properties derived from the diffusion tensor in the linear elastic model for non-rigid registration. First, we deformed a fiber phantom isotropically, where the entire volume deformed evenly, and anisotropically, where the fibers maintained their structure and the surrounding regions deformed. This showed that by calculating the local stiffness parameters at each location, we are able to automatically adjust the deformation to behave in a way consistent with what we know of the structure.

For the surgical cases in which DT-MRI data was acquired, the volumetric deformation was applied using both the isotropic and anisotropic linear elastic models. To evaluate the performance of the registration algorithm while varying the maximum ratio of stiffness along and across fibers, we used a set of landmarks identified by a neurosurgeon in both the preoperative and intraoperative image for one surgical case. These landmarks include the medial tumor margin, 3 points on the lateral temporal lobe surface, and the optic tract. A maximum stiffness ratio of 10 was optimal, but the displacement error differences were very small and the set of landmarks was limited.

The error in landmark displacements for the anisotropic model was then compared to that of the isotropic model and of the original rigid registration. The average for

each was 2.761 mm (anisotropic), 2.806 mm (isotropic),and 2.984 (rigid). Again, these differences are small, but the anisotropic model does show slight improvement.

To account for displacement differences that occurred where there were no landmarks identified, we compared the deformation fields directly. We began with a qualitative analysis of the difference images derived from the deformation fields and found that most of the displacement differences occur, as expected, in regions of high anisotropy. Quantitatively, the differences in displacement was between 1 and 3 mm for each surgical case, which is up to nearly 25% of the total maximum displacement due to brain shift.

Finally, we showed that the computation time required for the anisotropic model was approximately twice that of that of the isotropic model, but still on the order of about three minutes. Because the other registration steps require almost 10 minutes to complete, this additional time should not be an obstacle in using the software during the procedure.

7.2 Contributions

Overall, the goal of this thesis was to extend the current implementation of the non-rigid registration algorithm [6] to incorporate the underlying structure of the brain tissue into the biomechanical model, while still maintaining the ability to use the results of the registration in near real-time.

The registration software [38] was extended to make it possible to apply the deformation field, calculated from the volumetric deformation of the model, to DT-MRI images. Visualizations of the deformed DT-MRI and white matter structure are then available in addition to the MRI, MRA, fMRI volumes and models.

The linear elastic Finite Element model implementation was extended to allow for inhomogeneity and anisotropy according to the diffusion tensor data. DT-MRI provided magnitude and directional information of the diffusion of water, which has been shown to correspond to the anisotropy of brain tissue. Elasticity parameters are calculated at each tetrahedron in the mesh from the degree of anisotropy of the

corresponding voxels, the direction of the anisotropy, and input material parameter estimates.

After verification of the model with synthetic data, the registration algorithm was applied to several surgical cases retrospectively. From the results of those cases, the elasticity parameter estimates were optimized. Finally, the registration results were compared to those of the isotropic linear elastic model in order to evaluate the amount, if any, of improvement made by extending the model.

7.3 Perspectives and Future Work

There are several avenues that can be pursued to extend upon this work. First, there should be additional verification and evaluation of the model with more surgical cases, particularly those with larger amounts of brain shift. Identification of a greater number of landmarks would provide greater confidence in the registration accuracy differences. Additionally, a DT-MRI scan acquired at the end of the procedure would make it possible to compare the actual deformation of the white matter tracts to the model's prediction.

Next, the relationship that we define between the anisotropic tissue stiffness and the diffusion tensor is a simple linear mapping based on the fractional anisotropy. This is likely not how the diffusion tensor and the elasticity parameters are related, and more comprehensive studies could be used to improve this calculation. Intraoperative measurement of brain material properties would also allow for a more accurate modeling.

The model itself could also be extended to use the more complex material equations described in the related work in Chapter 2. As more powerful computers become available, these models become computationally feasible even given the time constraints of the neurosurgical procedure. Finally, the segmentation, rigid registration, and surface matching have become the slowest portion of the registration algorithm. Improvements here, in both computation time and accuracy, would further improve the registration.

Bibliography

[1] D. C. Alexander, C. Pierpaoli, P. J. Basser, and J. C. Gee. Spatial transformations of diffusion tensor magnetic resonance images. *IEEE Transactions on Medical Imaging*, 20(11):1131–1139, 2001.

[2] J. Braun, G. Buntkowsky, J. Bernarding, T. Tolxdorff, and I. Sack. Simulation and analysis of magnetic resonance elastography wave images using coupled harmonic oscillators and gaussian local frequency estimation. *Magnetic Resonance Imaging*, 19:703–713, 2001.

[3] L. Cohen and I. Cohen. Finite element methods for active contour models and balloons for 2d and 3d images. *IEEE Transactions on Pattern Analysis and Machine Intelligence*, 15:1131–1147, 1993.

[4] C. Davatzikos. Spatial transformation and registration of brain images using elastically deformable models. *Computer Vision and Image Understanding*, 66(2):207–222, 1997.

[5] A. Ding, J. C. Gore, and A. W. Anderson. Classification and quantification of neuronal fiber pathways using diffusion tensor mri. *Magnetic Resonance in Medicine*, 49:716–721, 2003.

[6] M. Ferrant. *Physics-based deformable modeling of volumes and surfaces for medical image registration, segmentation and visualization.* PhD thesis, Université Catholique de Louvain, April 2001.

[7] M. Ferrant, A. Nabavi, B. Macq, P. M. Black, F. A. Jolesz, R. Kikinis, and S. K. Warfield. Serial registration of intraoperative mr images of the brain. *Medical Image Analysis*, 6:337–359, 2002.

[8] M. Ferrant, A. Nabavi, B. Macq, F. A. Jolesz, R. Kikinis, and S. K. Warfield. Registration of 3-d intraoperative mr images of th brain using a finite-element biomechanical model. *IEEE Transactions on Medical Imaging*, 20(12):1384–1397, December 2001.

[9] L. R. Frank. Characterization of anisotropy in high angular resolution diffusion-weighted mri. *Magnetic Resonance in Medicine*, 47:1083–1099, 2002.

[10] D. T. Gering, A. Nabavi, R. Kikinis, N.. Hata, L. J. O'Donnell, W. E. Grimson, F. A. Jolesz, P. McL. Black, and W. M. Wells III. An integrated visualization system for surgical planning and guidance using image fusion and an open mr. *Journal of Magnetic Resonance Imaging*, 13:967–975, 2001.

[11] A. Guimond, C. R. G. Guttmann, S. K. Warfield, and C.-F. Westin. Deformable registration of dt-mri data based on transformation invariant tensor characteristics. In *Proceedings of the IEEE International Symposium on Biomedical Imaging*, July 2002.

[12] A. Hagemann, K. Rohr, H. S. Stiehl, U. Spetzger, and J. M. Gilsbach. Biomechanical modeling of the human head for physically based, nonrigid image registration. *IEEE Transactions on Medical Imaging*, 18(10):875–884, October 1999.

[13] R. F. S. Hearmon. *An Introduction to Applied Anisotropic Elasticity.* Oxford University Press, 1961.

[14] D. L. G. Hill, P. G. Batchelor, M. Holden, and D. J. Hawkes. Medical image registration. *Physics in Medicine and Biology*, 46:R1–R45, 2001.

[15] B. Morrison III, D. F. Meaney, and T. K. McIntosh. Mechanical characterization of an in vitro device designed to quantitatively injure living brain tissue. *Annals of Biomedical Engineering*, 26:381–390, 1998.

[16] C. R. Maurer Jr., J. M. Fitzpatric, M. Y. Wang, Jr. R. L. Galloway, R. J. Maciunas, and G. S. Allen. Registration of head volume images using implantable fiducial markers. *IEEE Transactions on Medical Imaging*, 16(4):447–462, 1997.

[17] G. Kindlmann, D. Weinstein, and D. Hart. Strategies for direct volume rendering of diffusion tensor fields. *IEEE Transactions on Visualization and Computer Graphics*, 6(2):124–138, 2000.

[18] J. Kozak, M. Nesper, M. Fischer, T. Lutze, A. Göggelmann, S. Hassfeld, and T. Wetter. Semiautomated registration using new markers for assessing the accuracy of a navigation system. *Computer Aided Surgery*, 7:11–24, 2002.

[19] S. Lee, G. Fichtinger, and G. S. Chirikjian. Numerical algorithms for spatial registration of line fiducials from cross-sectional images. *Medical Physics*, 29(8):1881–1891, August 2002.

[20] C.-P. Lin, W.-Y. I. Tseng, H.-C. Cheng, and J.-H. Chen. Validation of diffusion tensor magnetic resonance axonal fiber imaging with registered manganese-enhanced optic tracts. *NeuroImage*, 14:1035–1047, 2001.

[21] F. Maes and A. Collignon. Multimodality image registration by maximization of mutual information. *IEEE Transactions on Medical Imaging*, 16, 1997.

[22] M. Miga, K. Paulsen, F. Kennedy, J. Hoopes, A. Hartov, and D. Roberts. Initial in-vivo analysis of 3d heterogeneous brain computations for model-updated image-guided neurosurgery. In *MICCAI*, pages 743–752, 1998.

[23] M. I. Miga. A new approach to elastography using mutual information and finite elements. *Physics in Medicine and Biology*, 48:467–480, 2003.

[24] M. I. Miga, K. D. Paulsen, P. J. Hoopes, F. E. Kennedy, A. Hartov, and D. W. Roberts. In vivo modeling of interstitial pressure in the brain under surgical load using finite elements. *Transactions of the ASME*, 122:354–363, August 2000.

[25] M. I. Miga, K. D. Paulsen, J. M. Lemery, S. D. Eisner, A. Hartov, F. E. Kennedy, and D. W. Roberts. Model-updated image guidance: Initial clinical experiences with gravity-induced brain deformation. *IEEE Transactions on Medical Imaging*, 18(10):866–874, October 1999.

[26] K. Miller. Constitutive model of brain tissue suitable for finite element analysis of surgical procedures. *Journal of Biomechanics*, 32:531–537, 1999.

[27] K. Miller and K. Chinzei. Constitutive modelling of brain tissue: Experiment and theory. *Biomechanics*, 30(11/12):1115–1121, 1997.

[28] K. Miller and K. Chinzei. Mechanical properties of brain tissue in tension. *Journal of Biomechanics*, 35:483–490, 2002.

[29] K. Miller, K. Chinzei, G. Orssengo, and P. Bednarz. Mechanical properties of brain tissue in-vivo: Experiment and computer simulation. *Journal of Biomechanics*, 33:1369–1376, 2000.

[30] X. Papademetris. *Estimation of 3D Left Ventricular Deformation from Medical Images Using Biomechanical Models.* PhD thesis, Yale University, May 2000.

[31] G. J. M. Parker, C. A. M. Wheeler-Kingshott, and G. J. Barker. Distributed anatomical brain connectivity derived from diffusion tensor imaging. In *IPMI*, pages 106–120, 2001.

[32] M. T. Prange and S. S. Margulies. Regional, directional, and age-dependent properties of the brain undergoing large deformation. *Transactions of the ASME*, 124:244–252, April 2002.

[33] J. Rexilius. Physics-based nonrigid registration for medical image analysis. Master's thesis, Medical University of Luebeck, September 2001.

[34] F. B. Sachse, C. Henriques, G. Seemann, C. Riedel, C. D. Werner, R. C. Penland, B. Davis, and E. Hsu. Modeling of fiber orientation in the ventricular

myocardium with mr diffusion imaging. *Computers in Cardiology*, 28:617–620, 2001.

[35] E. Samset and H. Hirschberg. Neuronavigation in intraoperative mri. *Computer Aided Surgery*, 4:200–207, 1999.

[36] J. S. Shimony, R. C. McKinstry, E. Akbudak, J. A. Aronovitz, A. Z. Snyder, N. F. Lori, T. S. Cull, and T. E. Conturo. Quantitative diffusion tensor anisotropy brain mr imaging: normative human data and anatomic analysis. *Radiology*, 212:770–784, 1999.

[37] L. Z. Shuck and S. H. Advani. Rheological response of human brain tissue in shear. *Journal of Basic Engineering*, pages 905–911, December 1972.

[38] A. Tei. Multi-modality image fusion by real-time tracking of volumetric brain deformation during image guided neurosurgery. Master's thesis, Massachusetts Institute of Technology, February 2002.

[39] E. E. W. van Houten, K. D. Paulsen, M. I. Miga, F. E. Kennedy, and J. B. Weaver. An overlapping subzone technique for mr-based elastic property reconstruction. *Magnetic Resonance in Medicine*, 42:779–786, 1999.

[40] W. M. Wells, P. Viola, H. Atsumi, S. Nakajima, and R. Kikinis. Multi-modal volume registration by maximization of mutual information. *Medical Image Analysis*, pages 35–51, March 1996.

[41] D. J. Werring, C. A. Clark, G. J. M. Parker, D. H. Miller, A. J. Thompson, and G. J. Barker. Direct demonstration of both sturcture and function in the visual system: Combining diffusion tensor imaging with functional magnetic resonance imaging. *NeuroImage*, 9:352–361, 1999.

[42] J. D. West, K. D. Paulsen, S. Inati, F. Kennedy, A. Hartov, and D. W. Roberts. Incorporation of diffusion tensor anisotropy in brain deformation models for updating preoperative images to improve image-guidance. In *International Symposium on Biomedical Imaging*, pages 509–512, 2002.

[43] B. Westermann and R. Hauser. Online head motion tracking applied to the patient registration problem. *Computer Aided Surgery*, 5:137–147, 2000.

[44] C.-F. Westin, S. E. Maier, H. Mamata, A. Nabavi, F. A. Jolesz, and R. Kikinis. Processing and visualization for diffusion tensor mri. *Medical Image Analysis*, 6:93–108, 2002.

[45] M. R. Wiegell, H. B. W. Larsson, and V. J. Wedeen. Fiber crossing in human brain depicted with diffusion tensor mr imaging. *Radiology*, 217:897–903, 2000.

[46] A. Yezzi, A. Tsai, and A. Willsky. Medical image segmentation via coupled curve evolution equatiosn with global constraints. *Mathematical Methods in Biomedical Image Analysis*, pages 12–19, 2000.

[47] O. C. Zienkewickz and R. L. Taylor. *The Finite Element Method*, volume 1. McGraw-Hill Book Company, 4 edition, 1987.